https://doi.org/10.5194/egusphere-2026-943
Preprint. Discussion started: 24 February 2026

Data-Driven Enhancement of Ocean Surface Forcing for Accurate Floating Debris Transport Modelling in the East/Japan Sea

Hong T. M. Tran[1], Young G. Park[2], Jun M. Choi[3*]

[1]Fluid Mechanics Department, Faculty of Civil Engineering, Ho Chi Minh City University of Technology, Vietnam National University Ho Chi Minh City, Ho Chi Minh City, 700000, Vietnam
[2]Ocean Circulation and Climate Research Center, Korea Institute of Ocean Science and Technology, Busan, 49111, Republic of Korea
[3]Department of Ocean Engineering, College of Environment and Marine Sciences and Technology, Pukyong National University, Busan, 48513, Republic of Korea

Correspondence to: Jun M. Choi (jmchoi@pknu.ac.kr)

Abstract. The accumulation of floating debris is a growing concern in marginal seas. This study presents the largest surface drifter experiment conducted to date in the East/Japan Sea, utilizing 33 GPS-tracked drifters to calibrate particle tracking models. Deployed off the Korean coast in late fall 2021, the drifters revealed a clear transport conduit to the Japanese coastline, with beaching occurring after an average of 37 to 50 days. We systematically evaluated model performance driven by combinations of geostrophic currents, Ekman currents, Stokes drift, and windage using MAE and NCLS metrics. The results indicate that near-surface debris is best modelled by combining geostrophic currents, Stokes drift, and windage, whereas deeper debris (2-m depth) requires the additional inclusion of Ekman currents. These optimized forcing combinations were found to outperform global circulation models such as HYCOM and CMEMS. Furthermore, seasonal experiments revealed that strong winter winds accelerate eastward transport and beaching along the Japanese coast, while weaker summer winds allow mesoscale eddies to broaden dispersion zones across both Korean and Japanese coastlines. Validated by this extensive dataset, these findings enable more accurate tracking of floating debris in similar basins.

1 Introduction

Millions of tons of plastic debris enter the ocean annually, posing a significant threat to marine ecosystems and human health. This debris accumulates in eddies and gyres (Lebreton, 2022; Maximenko et al., 2012; Thiel et al., 2018), washes ashore on coastlines (Chenillat et al., 2021; Cole et al., 2011; Cózar et al., 2014; Dobler et al., 2022; Nakakuni et al., 2024), and fragments into smaller pieces that disperse widely over time. These fragments pose serious risks to marine life through ingestion, particularly for species with vast foraging and migration ranges (Clark et al., 2023; Santos de Moura et al., 2020). Because plastic debris can facilitate disease transmission, damage critical habitats like coral reefs (Pinheiro et al., 2023), impact human health (Paul et al., 2024), disrupt food chains (Saeedi, 2024), and alter ecosystem dynamics (Tekman et al.,

https://doi.org/10.5194/egusphere-2026-943
Preprint. Discussion started: 24 February 2026

2022), accurate modeling to track the trajectories, distributions, and accumulation of floating plastic debris is urgently needed.

Particle Tracking Models (PTMs) have been widely implemented to model the transport and fate of floating materials (Lebreton et al., 2012; Onink et al., 2019). Such models have also been extended to study plastic debris dispersion in rivers discharging into the Indian Ocean (Irfan et al., 2024). Within marginal seas, PTM applications include tracking floating particle trajectories influenced by subsurface currents in the Gulf of Mexico (Liang et al., 2021), modeling oil particle pathways following the Deepwater Horizon oil spill (Mariano et al., 2011), tracking plastics in the Mediterranean Sea using surface currents and Stokes drift (Liubartseva et al., 2018), predicting particle trajectories in the Adriatic Sea (Castellari et al., 2001), simulating oil spill diffusion in the Sea of Okhotsk (Ono et al., 2013), and predicting surface debris movement in the East/Japan Sea (EJS) (Iwasaki et al., 2017).

PTMs are typically driven by Eulerian surface currents, which are heavily influenced by a combination of geostrophic currents, Ekman transport, Stokes drift, and windage (Röhrs et al., 2023; Sebille et al., 2020). Geostrophic currents, resulting from the balance between the Coriolis force and horizontal pressure gradients (Sudre et al., 2013), play a fundamental role in long-term ocean circulation and influence both surface and subsurface flows globally. Wind directly affects floating objects by exerting force on their exposed surface area, known as windage, often quantified by wind drift factors ranging from 0 to 5% of the wind speed (Gu et al., 2024; Tamtare et al., 2022). Ekman transport, driven by wind stress and the Coriolis effect, generates a vertical current profile within the upper ocean layers (Bressan, 2019) and has been linked to microplastic accumulation in subtropical regions (Onink et al., 2019). The wave-induced current known as Stokes drift influences the direction and speed of surface currents, affecting the transport of floating objects (Mao & Heron, 2008; Tamtare et al., 2022). Consequently, a systematic study determining which physical processes dominate particle movement is crucial for model accuracy.

Drifter experiments are an essential tool for evaluating PTM results that simulate the transport and dispersion of floating plastic debris and the corresponding physical processes on the ocean surface. In open oceans, validation is often supported by massive datasets such as the Global Drifter Program, which maintains thousands of drifters globally (Lumpkin et al., 2017; Maximenko et al., 2012). With the exception of the massive CODE-type drifter experiment in the Gulf of Mexico (Poje et al., 2014; D'Asaro et al. 2018), drifter experiments in marginal seas are typically constrained in scale, often relying on a small number of drifters to investigate local transport features. For instance, recent studies in the North Sea used only 6 to 12 drifters to validate surface transport models (Callies et al., 2017; Medina-Rubio et al., 2026), and similar process-oriented studies in the East China Sea were conducted with as few as 4 to 29 SVP-type drifters (Hsu et al., 2021; Sun et al., 2022). Sotillo et al. (2016) compiled a CODE-type drifter dataset in the Strait of Gibraltar to validate ocean models and track contaminants. The primary role of these experiments is to validate the surface currents that directly affect the accuracy of the debris tracking model. However, many tracking model studies in marginal seas still lack validation with in-situ drift data, or employ drifter types that are not suitable for tracking floating debris. Here, we utilized 33 surface drifters deployed simultaneously, tracking currents at a depth of 0.3 m. Although this number is smaller than open-ocean campaigns, it

https://doi.org/10.5194/egusphere-2026-943
Preprint. Discussion started: 24 February 2026

represents one of the largest synoptic datasets conducted in a marginal sea and constitutes the largest surface drifter experiment conducted in the EJS.

We investigate transport and dispersion in the EJS using PTMs validated with drifter experiments. The EJS, a marginal sea approximately 1,000 km wide, is a recognized "hot spot" for microplastic accumulation (Isobe et al., 2015; Kuroda et al., 2024) and is often described as a "miniature ocean" due to its encapsulation of major global oceanic processes, such as deep water formation, thermohaline circulation, and mesoscale eddy activity, within a relatively small and semi-enclosed basin (e.g., Ichiye, 1984; Kim et al., 2001; Talley et al., 2006). Bordered by the Korean Peninsula, Japan, and the Russian Far East, the EJS receives a mix of natural and anthropogenic materials, including plastic debris, transported by ocean currents such as the Tsushima Warm Current, a branch of the Kuroshio Current flowing from the East China Sea, as well as by wind (Park et al., 2021). Although the transport and distribution of plastic debris in the EJS have been studied (Iwasaki et al., 2017; Kim et al., 2021; Takeda and Isobe, 2024), there remains a lack of observational data in this marginal sea validate particle trajectories and the specific physical processes influencing near-surface particle movement in the region.

In this study, we aimed to optimize the near-surface forcings that govern floating debris transport using a PTM validated with in-situ surface drifter observations. A drifter experiment was conducted to trace near-surface transport and assess the accuracy of simulated particle trajectories. In the results section, we identify the optimal combinations of key surface forcing components - geostrophic currents, Stokes drift, Ekman currents, and windage - for accurately modeling floating debris transport. By incorporating these forcings into the PTM, we simulated particle trajectories and compared them with observed drifter paths. In the discussion section, we evaluate the performance of the optimized forcing combinations relative to global ocean circulation models and further apply these combinations to estimate the seasonal variability of surface transport and beaching patterns of floating debris in the EJS.

2 Materials and Methods

2.1 Drifter experiment

Custom-made cylindrical drifters (Fig. 1a) were used to observe near-surface currents by tracking their movements in the EJS. The drifters, equipped with GPS trackers, were designed to collect location data at 5-minute intervals over several months. Each drifter measured 30 cm in height and 9 cm in diameter, with the top 3–5 cm protruding above the water surface when deployed. A total of 33 drifters were deployed, consisting of 23 undrogued drifters (hereafter referred to as DX drifters) and 10 drogued drifters (hereafter referred to as DO drifters). The drogue for the DO drifters consisted of two 30 cm × 30 cm plastic plates arranged perpendicularly and positioned at a depth of 2 m. By using surface drifters with slightly different depths, we aimed to investigate near-surface transport processes relevant to floating marine debris. Drifter positions were tracked from deployment until either beaching occurred or the signal was lost. The mean, minimum, maximum, and standard deviation of drifter lifetimes were 48.05, 12.2, 79.7, and 22.4 days, respectively. The location data were interpolated at 15-minute intervals and used for subsequent analysis.

We deployed drifters across the East Korea Warm Current (EKWC) in the EJS (Fig. 1). The current circulation in the eastern Korean peninsula is primarily driven by the northward-flowing EKWC and the southward-flowing North Korean Cold Current (NKCC), both of which are modulated by coastal currents, mesoscale eddies, and fronts (Lee et al., 2010). These flow systems generate dynamic pathways for drifters as they interact with local oceanographic features (Prants et al., 2011; Onink et al., 2019). Those drifters were deployed at six distinct deployment locations (inset in Fig. 1-b), and four DX drifters and either one or two DO drifters were released at each deployment location. The drifter deployment process commenced on November 10, 2021, at 01:40 UTC, with subsequent groups released at intervals, resulting in a total deployment duration of approximately 3 hours. Fig. 1-c and 1-d depict the geostrophic (pink vectors) and 1.5% of wind speed (black vectors) velocity fields averaged for the first month and the second month after release, respectively. At the initial deployment locations, a strong northward geostrophic current (0.22 m/s) and a eastward wind (10.0 m/s) were observed, and these conditions persisted in the monthly averaged fields (Fig. 1-c,d).

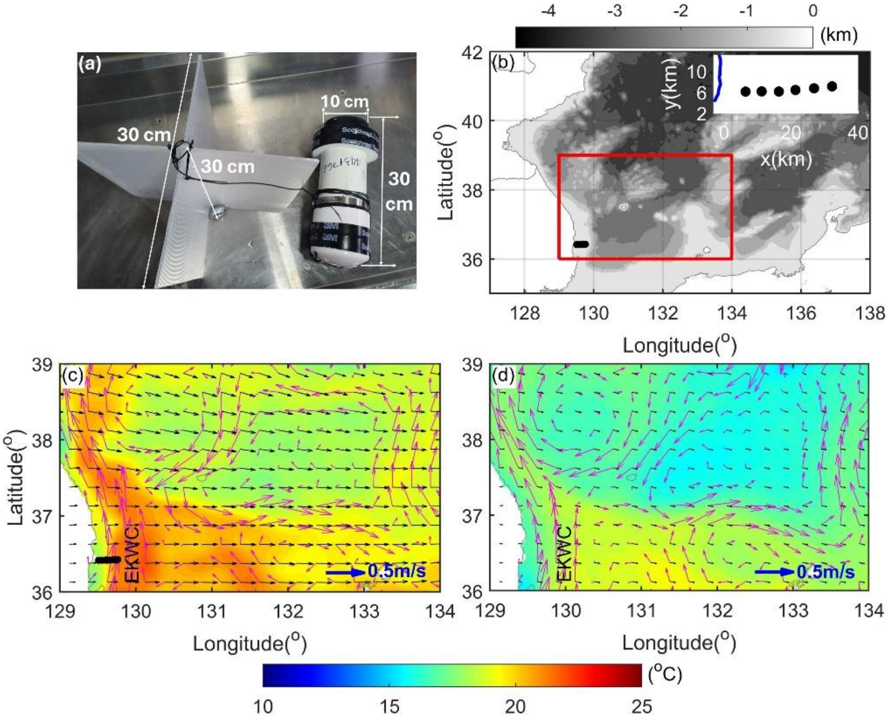

Figure 1. (a) Description of the drifter released in the East Korea Warm Current (EKWC). (b) Initial deployment locations of the drifters (black line in the red rectangle) with the inset image showing a detailed view of the initial locations, grouped into six deployment orders from east to west. The background color indicates bathymetry. (c) Geostrophic current (pink vectors) and 1.5% of the wind velocity at 10 m height (black vectors), with the background representing the sea surface temperature (SST) in the red rectangle shown in (b), averaged for one month from the deployment day (November 10, 2021). (d) Geostrophic current, wind velocity, and SST averaged for one month from December 10, 2021.

2.2 Ocean and atmosphere dataset

Four current components were considered to be associated with the movement of drifters: geostrophic current (Sudre et al., 2013; Tamtare et al., 2022), Ekman current (Sudre et al., 2013; Huang et al., 2021), Stokes drift (Curcic et al. 2016; Iwasaki et al. 2017; Parn et al. 2023), and windage (Gu et al., 2024). Geostrophic current ($\vec{u}_G$ or G), representing the background horizontal velocities, was obtained from the SEALEVEL_GLO_PHY_L4_MY_008_047 dataset, which provides daily global ocean observations at a spatial resolution of 0.125° and a temporal resolution of 1 day. Wind velocity at 10 m above the sea surface ($\vec{u}_{10}$) was obtained from the ECMWF Reanalysis v5 (ERA5) dataset, with a spatial resolution of 1/4° and a temporal resolution of 1 hour. The wind data were converted to wind stress using the bulk formula ($\vec{\tau} = \rho_a C_d \vec{u}_{10} |\vec{u}_{10}|$), where ρ_a is the air density, and $C_d (= 10^{-3}(0.8 + 0.065|\vec{u}_{10}|))$ is the drag coefficient (Chen et al., 2020; Wu, 1982; Cushman-Roisin et al., 2011; Rypina et al., 2021).

Stokes drift ($\vec{u}_S$ or S) was calculated using the University of Miami Wave Model, version 1.0.1 (UMWM), over the domain 125°E-135°E, 25°N-35°N, with a horizontal resolution of 0.0083° and 22 depth levels. The model was forced with daily wind data from ECMWF/ERA5 and ETOPO1 (Hersbach et al., 2020; Amante et al., 2009) bathymetry and coastline data. The three-dimensional Stokes drift fields were determined using the following equation:

$$\int_0^{2\pi} \int_0^{\infty} \omega k^2 \frac{cosh[2k(d+z)]}{2sinh^2 kd} F(f) dk d\theta \tag{1}$$

, where ω, *k, d, z*, θ, and *F* are the the angular frequency, wave number, mean water depth, the depth below the surface at which the Stokes drift is evaluated, the wave direction, and wavenumber variance spectrum, respectively (Haza et al., 2019) . The computation was performed for the period from November 10, 2021, to January 30, 2022. Significant wave height and Stokes drift data were saved daily during the computation period. The Ekman transport ($\vec{u}_E$ or E) was calculated using the following equations:

$$u_E = \frac{\sqrt{2}}{\rho f d} e^{\frac{z}{d}} \left[\tau_x cos\left(\frac{z}{d} - \frac{\pi}{4}\right) - \tau_y sin\left(\frac{z}{d} - \frac{\pi}{4}\right) \right] \tag{2}$$

$$v_E = \frac{\sqrt{2}}{\rho f d} e^{\frac{z}{d}} \left[\tau_x sin\left(\frac{z}{d} - \frac{\pi}{4}\right) - \tau_y cos\left(\frac{z}{d} - \frac{\pi}{4}\right) \right] \tag{3}$$

, where the Ekman layer depth $d = 3.2|\vec{u}_{10}|/(\sin(\phi))^{0.5}$, ρ is the water density, ϕ is the latitude, and z is water depth (Rypina et al., 2021). Furthermore, the sea surface temperature (SST) data were sourced from the GLOBAL_MULTIYEAR_PHY_001_030 product, which provides a spatial resolution of 0.0083° and a daily temporal resolution, and were used to examine stratification dynamics in the EJS.

2.3 The particle tracking model

The PTM was used to evaluate the accuracy of various combinations of surface forcing components by comparing the particle trajectory to the drifter trajectory. From the given horizontal velocity field ($\vec{u}$), the particle location can be estimated by a deterministic advection component and a stochastic diffusion component, as given by

$$\vec{x}(t + \Delta t) - \vec{x}(t) = \vec{u}\Delta t + R\sqrt{2K_h \Delta t} \tag{4}$$

, where $\vec{x}$ is the displacement vector of a Lagrangian particle, Δt is the time step in the PTM (here 1800s), R is a random number generated at each time step ormal distribution, and K_h is the horizontal diffusion coefficient from the Smagorinsky scheme (Irfan et al., 2024; Jalón-Rojas et al., 2019; Seo et al., 2020). The total current velocity ($\vec{u}$) was determined by a linear combination of the physical processes described in the previous section:

$$\vec{u} = \vec{u}_G + \vec{u}_S + \vec{u}_E + \vec{u}_W \tag{5}$$

, where $\vec{u}_G$, $\vec{u}_S$, $\vec{u}_E$, and $\vec{u}_W$ (= $r\vec{u}_{10}$) represent the geostrophic current (G), Stokes drift (S), Ekman current (E), and windage (W), respectively. These forcings were obtained from the datasets described in Section 2.2. The coefficient r given by

$$r = \sqrt{\rho_a C_{d,a} A_a / \rho_w C_{d,w} A_w} \tag{6}$$

, which represents the wind drag coefficient on the drifters, where ρ_a and ρ_w are the density of air and seawater, respectively, $C_{d,a}$ and $C_{d,w}$ are the drag coefficients for the surface drifters in air and seawater, respectively, and A_a and A_w denote the horizontally projected areas of the surface drifters above and below the water surface, respectively (Kako et al., 2010). The r values for DX and DO drifters were estimated as 0.015 and 0.005, respectively, falling within the 0% - 5% range reported in previous studies and reflecting the specific environmental conditions and drifter types used (Gu et al., 2024; Hui et al., 2023; Kako et al., 2010). Tidal currents were neglected in this study because they are relatively weak in the EJS (Jeon et al., 2014), and our result (not shown) confirmed that tidal forcing had a negligible effect on particle trajectories in the region.

Two sets of PTM simulations were conducted using eight combinations of current forcings described in Table 1: PTM-DX, driven by forcings sampled at the surface (z = 0 m) to simulate undrogued drifters (DX), and PTM-DO, driven by currents sampled at a depth of 1.5 m (z = -1.5 m) to simulate drogued drifters (DO). For the PTM-DX simulations, Stokes drift and Ekman current components were sampled at the surface, while for the PTM-DO simulations, these components were sampled at a depth of 1.5 m, which approximates the center of area considering both the cylindrical drifter and the drogue. To evaluate the optimal forcing combination, one particle was released from each drifter's initial location to simulate its trajectory, and each simulation was run for a period of 79 days, matching the longest observed drifter track.

2.4 Evaluation of the particle trajectory

The particle trajectories calculated from the PTM were compared with observed drifter trajectories to determine the optimal combination of forcing components representing near-surface currents. The Mean Absolute Error (MAE), and the Normalized Cumulative Lagrangian separation (NCLS) (Kim et al., 2023) were used as metric to quantify the difference between particle and drifter trajectories. The equation for the MAE is given by

$$MAE = \frac{1}{N}\sum_{i=1}^{N}(|\Delta Lon| + |\Delta Lat|) \tag{7}$$

, where ΔLon and ΔLat are the differences between longitude and latitude of the observed and predicted trajectories. N is the number of the dataset (Kim et al., 2023). Lower MAE values indicate more precise forecasts and better overall performance.

The NCLS is defined as the cumulative summation of the separation distance between the particle and drifter trajectories, weighted by the length of the drifter trajectories accumulated in time, as follow:

$$NCLS = \begin{cases} 1 - \frac{s}{n} & (NCLS \leq n) \\ 0 & (NCLS > n) \end{cases} \quad (8)$$

, where s ($= \sum_{i=1}^{N} D_i / \sum_{i=1}^{N} L_{o,i}$) denotes the normalized cumulative separation and n is a dimensionless value representing the allowed threshold. This study adopted a value of $n = 1$, consistent with the approach used by Kim et al., (2023), Liu et al., (2011) and Liu et al., (2014). D_i is the separation distance between drifter and particle trajectories at time step i, $L_{o,i}$ is the cumulative length of the observed trajectories at time step i. Thus, MAE and NCLS are the dimensional and nondimensional metrics, respectly, that measure the cumulative error between the simulated particle and observed drifter trajectories. NCLS values closer to 1 (with a range of 0 to 1) indicate a more accurate simulation.

2.5 Evaluation of the particle dispersion

Dispersion of the particle and drifter clusters were investigated using two metrics: the relative dispersion ($R^2(t)$) and the Finite-Scale Lyapunov Exponent (FSLE). The relative dispersion indicates the growth in size of the drifter cluster relative to its center of mass as given by

$$R^2(t) = \frac{1}{N} \sum_{i=1}^{N} [x_i(t) - x_{cm}(t)]^2 \quad (9)$$

, where N is the number of drifters, $x_i(t)$ is the position vector of the i-th drifter at time t, and $x_{cm}(t)$ is the position vector of the center of mass of the drifter cluster at time t (LaCasce, 2008). The corresponding dispersion coefficient (K) was estimated as

$$K = \frac{1}{4} \frac{\sigma_r^2}{t} \quad (10)$$

, where σ_r^2 is the radially symmetrical variance (Okubo, 1971; LaCasce, 2008). Different scaling regimes of $R^2(t)$ with time indicate different dispersion processes e.g., $R^2(t) \sim t$ for diffusive dispersion, $R^2(t) \sim t^3$ for Richardson dispersion, which correspond to $K \sim L^0$ and $K \sim L^{4/3}$, respectively, where L is $3\sigma_r$ represents the size of the particle cluster.

In addition to relative dispersion, the FSLE was also calculated to characterize the dispersion process. The FSLE (λ), measures the average rate of separation of initially nearby particles over a finite distance. It is calculated by tracking pairs of particles and measuring the time it takes for their separation to grow from an initial separation distance, δ_0, to a final separation distance, δ_f:

$$\lambda = \frac{1}{\langle \Delta t \rangle} ln \left(\frac{\delta_f}{\delta_0} \right) \quad (11)$$

, where Δt is the time it takes for the separation to grow from δ_0 to δ_f, and the angle brackets $\langle \rangle$ denote an average over all particle pairs (Aurell et al. 1996). A larger FSLE value indicates a faster rate of separation and thus stronger strain rate. Like the relative dispersion, difference scaling regimes of FSLE with respect to separation distance δ reveal different dispersion processes: $\lambda \sim \delta^{-1}$ for ballistic dispersion ($R^2(t) \sim t^2$), $\lambda \sim \delta^{-1/2}$ for Richardson-like dispersion ($R^2(t) \sim t^3$), and $\lambda \sim \delta^{-2}$ for diffusive dispersion ($R^2(t) \sim t$) (McWilliams, 2016).

3 Results, or a descriptive heading about the results

3.1 Drifter trajectory

All drifters deployed near the Korean coast, excluding those with signal loss, ultimately reached the Japanese coast within a period ranging from 13 to 68 days. Figure 2 shows the trajectories and final destinations of the DX drifters (a) and DO drifters (b), overlaid on maps of sea surface height, wind velocity vectors (cyan), and geostrophic current fields (white), time-averaged for November (Fig. 2a) and December (Fig. 2b). Within 12 hours of deployment, the drifters began diverging into two distinct pathways. One group, comprising 60% of the DO drifters and 27% of the DX drifters, moved northward along the eastern coast of Korea, influenced by the strong East Korea Warm Current (EKWC). The other group, consisting of 40% of the DO drifters and 73% of the DX drifters, drifted eastward toward the Japanese coast, primarily driven by prevailing westerly winds. This bifurcation in drifter trajectories is likely associated with a nearby hyperbolic point, defined as a location where stable and unstable manifolds intersect, partitioning the flow into distinct transport pathways and often inducing rapid separation of particle trajectories (Prants et al., 2015). This hyperbolic point was located near 130°E, 37.3°N (Fig. 2), corresponding to the observed divergence. The mean speeds of the DO and DX drifters were calculated as 0.28 m/s and 0.31 m/s, respectively.

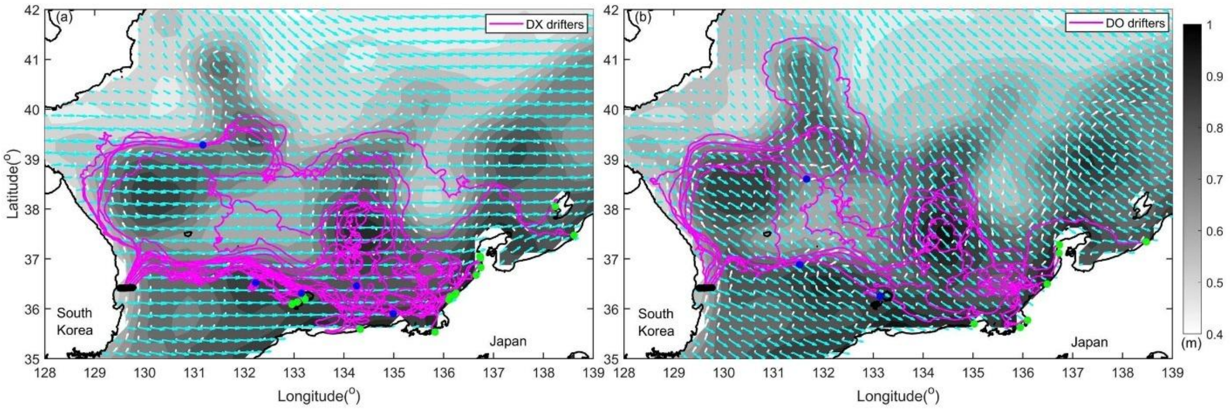

Figure 2. Drifter trajectories for DX (a) and DO (b) drifters. The background shows the absolute dynamic topography, and the vector field indicates geostrophic current (black vectors) and wind (cyan vectors) in the EJS, as provided by the Copernicus Marine and Environment Monitoring Service and ECMWF Reanalysis v5, averaged for November 2021 (a) and December 2021 (b). Black thick lines indicate the initial deployment locations. Blue dots indicate the final locations of drifters that remained at sea, while green dots indicate the locations where drifters landed on the Japanese coastline.

3.2 Drifter dispersion

The time evolution of the relative dispersion, $D^2(t)$ (Eq. 9), and the dispersion coefficient, $K(L)$ (Eq. 10), for the drifters is illustrated in Fig. 3. At very early times (t < 0.3 days) and small length scales (L < 1 km), the drifter cluster exhibited diffusive dispersion ($D^2 \sim t^1$). Beyond this initial stage, Richardson dispersion ($D^2 \sim t^3$, or equivalently, $K^2 \sim L^{4/3}$), was evident in the range of approximately 0.3 to 30 days, corresponding to length scales from L = 1 km to 100 km. During 0 < t < 3 (or L < 60 km), the DO drifters showed slightly greater dispersion than DX drifters, which was possibliy attributed to the different passages determined at the hyperbolic point. The majority of DO drifters followed passage along the EKWC near the Korean coastline, where horizontal shear in the coastal current can enhance the dispersion. In contrast, the majority of DX drifters moved offshore, where the transport was dominated by spatially uniform wind in a narrow directional range, resulting in relatively weaker dispersion during the time. However, after approximately 3 days, as the DX drifters moved farther offshore, interactions with mesoscale eddies in the westerly downwind regions enhanced their dispersion, leading to super-Richardson behavior and causing their relative dispersion to exceed that of the DO drifters.

The estimated dispersion coefficients for all drifters were approximately 1, 20, and 1,000 m^2/s at scales of 1, 10, and 100 km, respectively, eventually saturating around 2,000 m^2/s in the EJS. The dispersion coefficient at the early stage was comparable to previous dye and drifter experiments in various waters, including coastal regions, inland waters, and open oceans (Okubo, 1971; Choi et al., 2019; Kim et al., 2024). For scales of 1–100 km, the growth in dispersion followed trends observed in open oceans, and the coefficient saturated when the length scale of the drifter cloud reached approximately 1/10 of the basin scale of the EJS (~2,000 km).

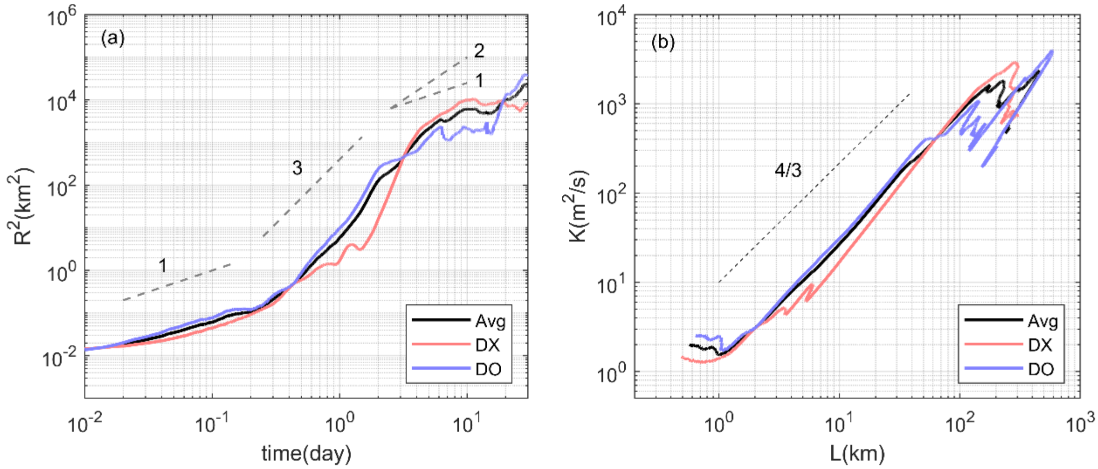

Figure 3. Relative dispersion ($R(t)^2$) (a) and dispersion coefficient ($K(L)$) (b) of the observed drifters. Panel (a) shows the time evolution of relative dispersion ($R(t)^2$), and panel (b) shows the dispersion coefficient ($K(L)$) as a function of length scale. The red line represents the undrogued (DX) drifters, the blue line represents the drogued (DO) drifters, and the black line indicates the average dispersion of all drifters (both DX and DO).

The FSLE values and trends for both DX and DO drifters were generally similar, but the FSLE values for DO drifters were slightly higher, particularly at very early times at spatial scales on the order of 10 meters and between 0.5 and 50 km. This pattern aligns with the dispersion coefficient K shown in Fig. 3b, where K is also larger for DO drifters over these scales. The difference in FSLE between DO and DX drifters is likely due to their distinct pathways delineated by the hyperbolic point, consistent with observations from the relative dispersion analysis. The FSLE curves reveal distinct dynamical regimes across spatial scales. In the small-scale regime ($\delta < 0.5\ km$), DX drifters exhibit a slope close to -1, indicative of ballistic dispersion, possibly associated with well-aligned wind-induced transport. In the submeso- and mesoscale-range ($1\ km < \delta < 50\ km$), the slope for DX drifters becomes slightly gentler, and FSLE values remain lower than those of DO drifters. For DO drifters, the FSLE initially shows a steep slope near -2 at small scales ($\delta < 0.5\ km$), characteristic of a diffusive regime, then transitions to a slope of approximately -1/2 to -2/3, reflecting Richardson-like dispersion (Fig. 4). This behavior is consistent with the influence of coastal currents and mesoscale eddy interactions in the region. At larger scales (beyond ~150 km), both DX and DO drifters show a steepening of FSLE values again, corresponding to the scale of mesoscale eddies in the EJS.

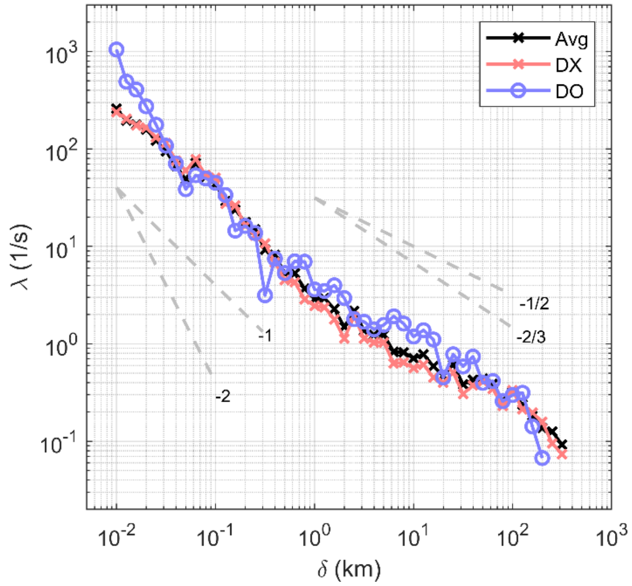

Figure 4. Finite-Size Lyapunov Exponent (FSLE), λ, as a function of separation distance, δ, for the observed drifters. The black line represents the average of all drifters, the red line represents the undrogued (DX) drifters, and the blue line represents the drogued (DO) drifters. The dashed gray lines indicate reference slopes of -2, -1, -1/2, and -2/3.

3.3 Particle trajectory

The performance of the forcing combinations detailed in Fig. 1 was evaluated by qualitatively comparing the observed drifter trajectories with simulated particle trajectories at two different depths: DX drifters were compared with PTM-DX particles driven by surface forcings (Fig. 5), while DO drifters were compared with PTM-DO particles driven by subsurface forcings at 1.5 m depth (Fig. 6). For the PTM-DX particles, increasing the number of forcing components improved the model's ability to replicate the bifurcation of drifter trajectories at the hyperbolic point, particularly when windage was included (Fig. 5f–h). When simulations were driven solely by geostrophic currents (Fig. 5a), all particles drifted predominantly northward along the EKWC, ultimately accumulating in a mesoscale eddy centered near 132°E, 41°N. The addition of Ekman currents (Fig. 5b) did not result in significant differences. However, including Stokes drift (Fig. 5c) reduced the residence time of particles within the eddy and redirected them toward the Japanese coast. In all simulations without windage, particles remained confined along the EKWC, whereas simulations incorporating windage produced more realistic trajectories that aligned with observed DX drifter paths, which split into both coastal and offshore passages. For PTM-DO particles (Fig. 6), all forcing combinations resulted in transport along the EKWC. The variation among trajectories was less pronounced than for PTM-DX, indicating a stronger influence of the coastal current. Although none of the PTM-DO simulations captured the bifurcation at the hyperbolic point, the simulation including all four components, geostrophic currents, Ekman currents, Stokes drift, and windage (Fig. 6h), most closely reproduced the observed DO drifter trajectories.

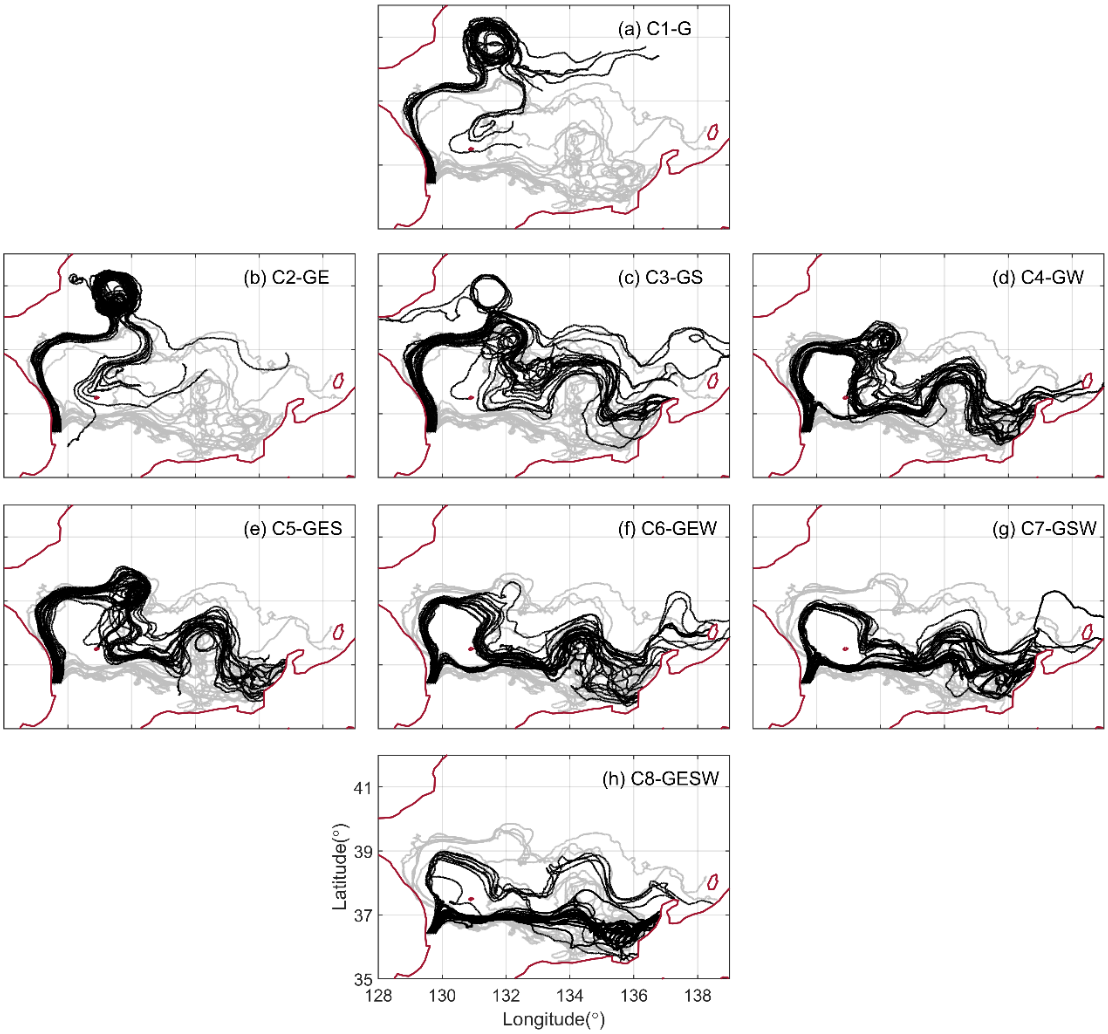

Figure 5. Particle trajectories using surface forcings (PTM-DX) simulated for 3 months. Panels (a-h) correspond to current 285 combinations C1-C8 as described in Table 1. Black lines represent the simulated PTM-DX particle trajectories, while gray lines represent the observed DX drifter trajectories for comparison. The panels are arranged by the number of forcing components included: the first row shows single-component forcing (a); the second row shows two-component forcings (b-d); the third row shows three-component forcings (e-g); and the fourth row shows the four-component forcing (h). G, E, S, and W indicate geostrophic current, Ekman current, Stokes drift, and windage forcings, respectively.

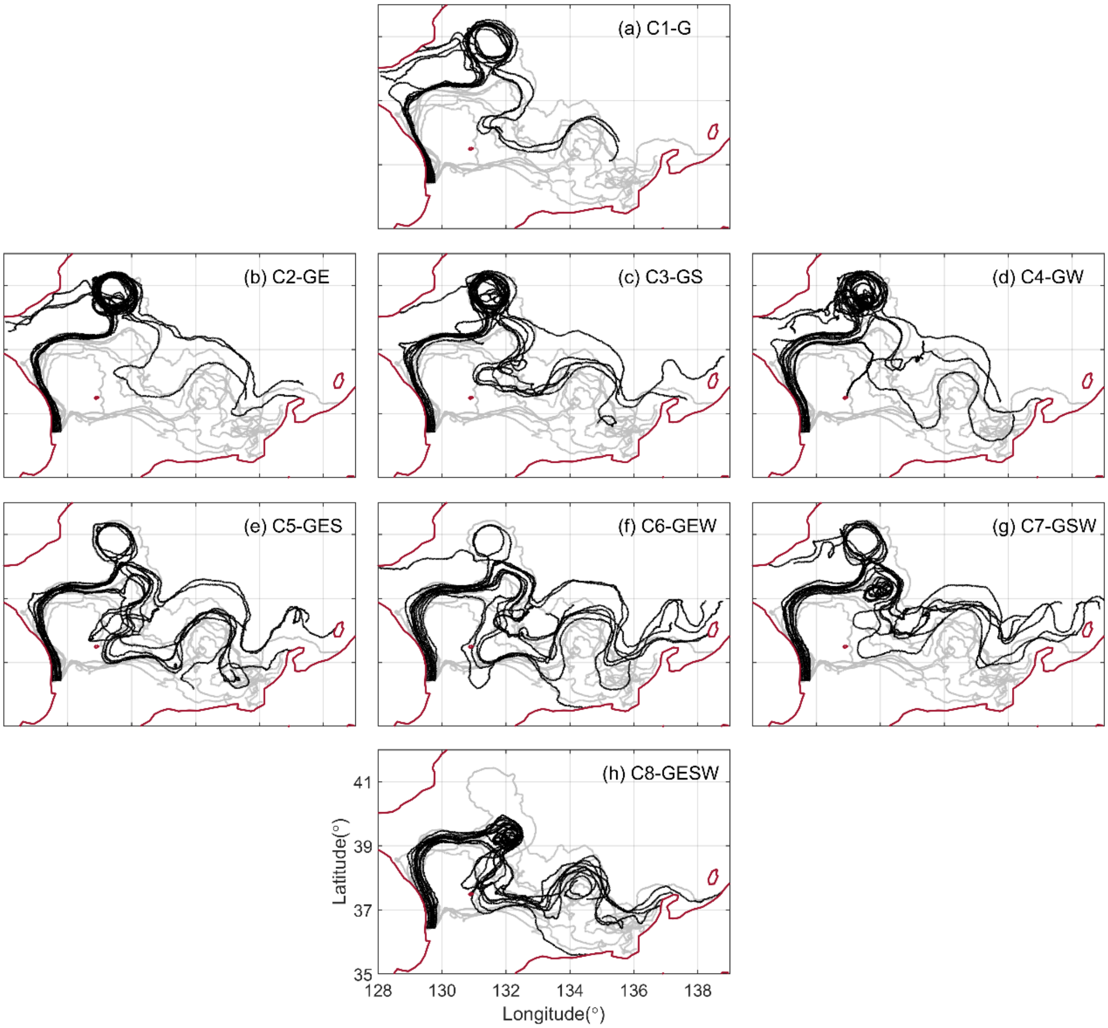

290

Figure 6. Particle trajectories using surface forcings (PTM-DO) simulated for 3 months. Panels (a-h) correspond to current combinations C1-C8 as described in Table 1. Black lines represent the simulated PTM-DO particle trajectories, while gray lines represent the observed DO drifter trajectories for comparison. The panels are arranged by the number of forcing components included: the first row shows single-component forcing (a); the second row shows two-component forcings (b-
295 d); the third row shows three-component forcings (e-g); and the fourth row shows the four-component forcing (h). G, E, S, and W indicate geostrophic current, Ekman current, Stokes drift, and windage forcings, respectively.

3.4 Particle dispersion

https://doi.org/10.5194/egusphere-2026-943
Preprint. Discussion started: 24 February 2026

Figure 7 presents the time evolution of relative dispersion, $D^2(t)$, for PTM-DX and PTM-DO particles under the eight forcing combinations (C1-C8). Overall, the two PTM sets exhibited comparable dispersion magnitudes and slopes; however, notable differences arose when windage was included. In cases where windage was applied (Fig. 7d and 7f-h), PTM-DX particles exhibited greater dispersion than PTM-DO particles, contrary to the drifter observations, which showed that DO drifters experienced higher dispersion, particularly at mesoscale distances. This discrepancy stemmed from the model's failure to reproduce the bifurcation at the hyperbolic point. In the observations, both DX and DO drifters split between an offshore path and the EKWC path, albeit with different proportions: more DX drifters followed the offshore route, while more DO drifters remained along the EKWC, where coastal shear enhanced dispersion. In contrast, the simulations confined all PTM-DO particles to the EKWC path, while PTM-DX particles were distributed between both paths. Since particles restricted to the EKWC path experience weaker dispersion compared to those traversing both the EKWC and offshore routes, the PTM-DO simulations underestimated dispersion relative to PTM-DX, opposite to the pattern observed in the drifter data.

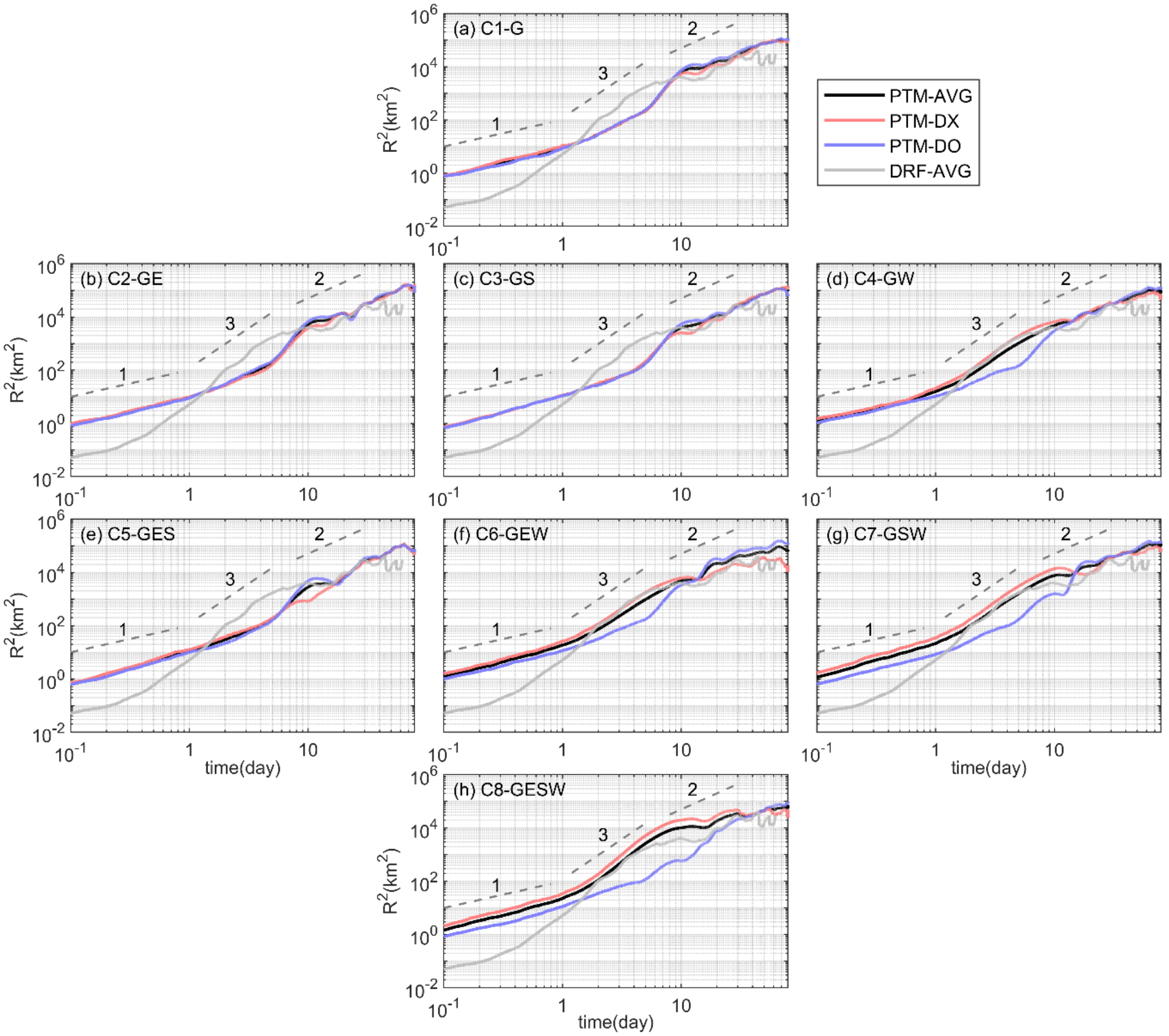

Figure 7. Relative dispersion ($R^2(t)$) of particles simulated with different forcing combinations (C1-C8) as described in Table 1, shown alongside observed drifter dispersion. Panels are arranged in the same order as in Fig. 5 and 6. Red and blue lines represent the relative dispersions for PTM-DX and PTM-DO simulations, respectively, and the gray line represents the average relative dispersion of the observed drifters for comparison. G, E, S, and W indicate geostrophic current, Ekman current, Stokes drift, and windage forcings, respectively.

Both particles and drifters exhibited a diffusive phase during the early stages; however, this phase persisted only briefly for the drifters (for t<0.3), while it extended significantly longer for the particles (up to approximately 2 days), until the average pairwise separation distance reached 25 km, the model's grid resolution. As a result, the effective diffusivity of particle pairs separated by less than 25 km was substantially higher than that observed in the drifter data. This discrepancy arises from the Smagorinsky scheme, which applies a constant diffusion coefficient within each 25 km grid cell, leading to

https://doi.org/10.5194/egusphere-2026-943
Preprint. Discussion started: 24 February 2026

artificially enhanced diffusion at very early times in all PTM simulations. The domain-averaged horizontal diffusion coefficient during the drifter observation period (November 2021 to February 2022), computed using the Smagorinsky parameterization, was approximately 87.3 m^2/s. This value is consistent with the empirical, scale-dependent horizontal diffusivity described by Okubo (83.7 m^2/s), given by $K = 0.0103L^{1.15}$, where K is in cm^2/s and L is the spatial scale in cm. In this context, L is taken as $3\sigma_r$, or equivalently $3\Delta x$, with Δx = 25 km representing the grid size.

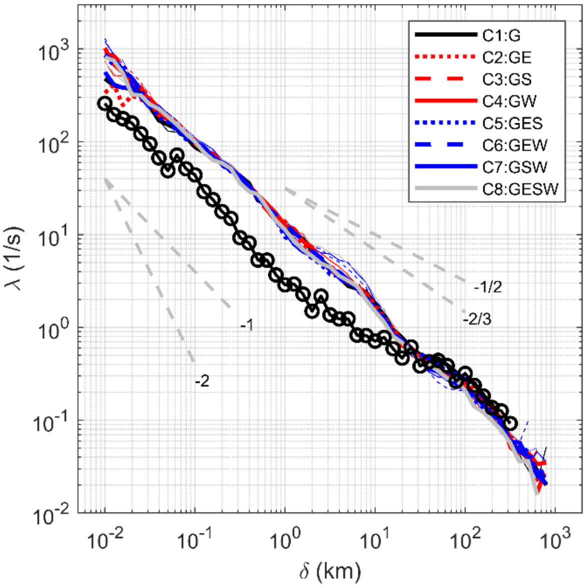

Figure 8. Finite-Size Lyapunov Exponent (FSLE), λ, as a function of separation distance, δ, for the simulated particles and observed drifters. The black line with circles represents the FSLE averaged for all observed drifters. Other colored lines show FSLEs for simulated particles from different forcing combinations (C1-C8, as listed in Table 1). Thinner lines indicate PTM-DX simulations, and thicker lines indicate PTM-DO simulations. The variation in FSLE values between different forcing combinations and between PTM-DX and PTM-DO were small.

The FSLE (λ) for the particle simulations (C1-C8) showed only minor differences among the various forcing combinations (Fig. 8). FSLE values from simulated particles and observed drifters became comparable at spatial scales greater than approximately 25 km, which aligns closely with the spatial grid size used for the current data in the simulations. At scales smaller than approximately 25 km, the FSLEs of the simulated particles were roughly three times greater than those observed from real drifters. This disparity at smaller scales occurs because particles in simulations are initially confined within grid cells, influenced significantly by numerical diffusion inherent in the Smagorinsky scheme. At these early times and small scales, the FSLE slopes for the drifters and particles are approximately -1, indicative of a ballistic dispersion regime. At intermediate spatial scales between about 25 km and 200 km, the FSLE curves for the simulated particles exhibit a slope closer to -1/2, signifying a local dispersion regime. Beyond roughly 200 km, the FSLE slopes steepen, approaching a slope of about -5/4, particularly evident in simulations where many particles eventually reach the coastline.

3.5 Evaluation of particle trajectory

The values of MAE (Eq. 7) and NCLS (Eq. 8) at different time steps are presented in Tables 3 and 4, respectively. The values in parentheses in both tables represent the ratio of each metric relative to the best-performing forcing combination for the corresponding time step. Thus, a larger ratio for MAE or a smaller ratio for NCLS indicates relatively poorer accuracy. The trends in MAE and NCLS across the various forcing combinations were generally consistent. Simulations using only the geostrophic current (C1) consistently exhibited the lowest accuracy for both PTM-DX and PTM-DO particle cases. Incorporating three current components typically improved accuracy compared to simulations with two components; however, the addition of all four current components did not necessarily yield optimal performance for the PTM-DX particles.

		C1	C2	C3	C4	C5	C6	C7	C8
	day	u_G	u_{G+E}	u_{G+S}	u_{G+W}	u_{G+E+S}	u_{G+E+W}	u_{G+S+W}	$u_{G+E+S+W}$
PTM-DX	1	22.7 (2.1)	23.2 (2.1)	18.6 (1.7)	15.2 (1.4)	18.4 (1.7)	14.9 (1.4)	**10.8 (1.0)**	11.1 (1.0)
	5	134.5 (6.1)	107.3 (4.9)	122.7 (5.6)	90.0 (4.1)	106.1 (4.8)	57.0 (2.6)	**22.0 (1.0)**	19.3 (0.9)
	10	251.4 (10.4)	242.6 (10.1)	221.1 (9.2)	166.0 (6.9)	209.6 (8.7)	92.6 (3.8)	**24.1 (1.0)**	35.8 (1.5)
	30	475.8 (8.8)	460.7 (8.5)	308.6 (5.7)	209.0 (3.9)	265.6 (4.9)	92.0 (1.7)	**54.0 (1.0)**	91.0 (1.7)
	75	562.5 (7.6)	606.1 (8.2)	347.0 (4.7)	145.0 (2.0)	243.9 (3.3)	90.80 (1.2)	**73.8 (1.0)**	83.2 (1.1)
	avg.	289.4 (7.0)	288.0 (6.8)	203.6 (5.4)	125.0 (3.7)	168.7 (4.7)	69.5 (2.1)	**36.9 (1.0)**	48.1 (1.2)
PTM-DO	1	19.7 (1.3)	20.7 (1.3)	18.4 (1.2)	17.1 (1.1)	18 (1.2)	16.7 (1.1)	15.9 (1.0)	**15.4(1.0)**
	5	75.7 (1.4)	64.1 (1.2)	79.3 (1.4)	68.7 (1.2)	68.8 (1.2)	59.2 (1.1)	68.7 (1.2)	**55.3(1.0)**
	10	146.5 (1.4)	135.6 (1.3)	140.2 (1.3)	123.1 (1.2)	129.4 (1.2)	113.8 (1.1)	120.1 (1.1)	**107(1.0)**
	30	318.0 (2.9)	286.5 (2.6)	304.9 (2.8)	235.6 (2.1)	216.9 (2.0)	175.5 (1.6)	201.4 (1.8)	**110.7(1.0)**
	75	537.0 (2.9)	487.9 (2.6)	487.9 (2.6)	377.1 (2.0)	459.6 (2.5)	322.6 (1.7)	410.3 (2.2)	**185.2 (1.0)**
	avg.	219.4 (2.0)	199.0 (1.8)	206.1 (1.9)	164.3 (1.5)	178.5 (1.6)	137.6 (1.3)	163.3 (1.5)	**94.7 (1.0)**

Table 3. MAE values for undrogued particles (PTM-DX) and drogued particles (PTM-DO) under 467 different forcing combinations (C1–C8) over time. Lower MAE values indicate better model 468 performance. Bolded values represent the lowest MAE for each time step. Values in 469 parentheses show the ratio of each MAE to the lowest MAE for that time step, a ratio closer to 470 1 denotes better relative performance.

		C1	C2	C3	C4	C5	C6	C7	C8
	day	u_G	u_{G+E}	u_{G+S}	u_{G+W}	u_{G+E+S}	u_{G+E+W}	u_{G+S+W}	$u_{G+E+S+W}$
PTM-DX	1	0.49 (1.4)	0.52 (1.3)	0.59 (1.2)	0.67 (1.1)	0.62 (1.2)	0.70 (1.1)	0.78 (1.0)	**0.79 (1.0)**
	5	0.02 (2.0)	0.07 (1.9)	0.11 (1.9)	0.35 (1.6)	0.23 (1.7)	0.58 (1.3)	0.82 (1.0)	**0.85 (1.0)**
	10	0.00 (2.0)	0.00 (2.0)	0.00 (2.0)	0.13 (1.8)	0.00 (2.0)	0.51 (1.4)	**0.86 (1.0)**	0.80 (1.1)
	30	0.33 (1.6)	0.35 (1.6)	0.55 (1.4)	0.69 (1.2)	0.61 (1.3)	0.86 (1.1)	**0.91 (1.0)**	0.86 (1.1)
	75	0.63 (1.3)	0.60 (1.4)	0.77 (1.2)	0.90 (1.1)	0.83 (1.1)	0.94 (1.0)	**0.96 (1.0)**	0.96 (1.0)
	avg.	0.29 (1.7)	0.31 (1.6)	0.40 (1.5)	0.55 (1.4)	0.46 (1.5)	0.72 (1.2)	**0.87 (1.0)**	0.85 (1.0)
PTM-DO	1	0.56 (1.2)	0.56 (1.2)	0.59 (1.1)	0.63 (1.1)	0.62 (1.1)	0.65 (1.0)	0.65 (1.0)	**0.68 (1.0)**
	5	0.42 (1.3)	0.50 (1.1)	0.39 (1.3)	0.48 (1.2)	0.48 (1.2)	0.55 (1.1)	0.48 (1.2)	**0.58 (1.0)**
	10	0.24 (1.5)	0.29 (1.4)	0.28 (1.4)	0.36 (1.2)	0.34 (1.2)	0.41 (1.1)	0.37 (1.2)	**0.45 (1.0)**
	30	0.56 (1.3)	0.60 (1.3)	0.57 (1.3)	0.66 (1.2)	0.70 (1.2)	0.75 (1.1)	0.71 (1.1)	**0.83 (1.0)**
	75	0.67 (1.2)	0.70 (1.2)	0.70 (1.2)	0.77 (1.1)	0.72 (1.2)	0.80 (1.1)	0.74 (1.2)	**0.88 (1.0)**
	avg.	0.49 (1.3)	0.53 (1.2)	0.51 (1.3)	0.58 (1.2)	0.57 (1.2)	0.63 (1.1)	0.59 (1.1)	**0.68 (1.0)**

Table 4. NCLS values for undrogued particles (PTM-DX) and drogued particles (PTM-DO) for different forcing combinations (C1-C8) over time. Higher NCLS values indicate better model accuracy (values range from 0 to 1). Bolded values represent the highest NCLS for each time step. Values in parentheses represent the ratio of the NCLS to the highest NCLS for that time step, a ratio closer to 1 denotes better relative performance.

For PTM-DX, among the two-component combinations, adding the Ekman current to the geostrophic current (C2) yielded performance comparable to simulation with geostrophic current alone (C1). In contrast, adding windage (C4) significantly improved accuracy relative to adding Stokes drift (C3). Among the three-component combinations, the combination of Ekman current and Stokes drift (C5) produced the lowest accuracy, while the combination of Stokes drift and windage (C7) consistently delivered the highest accuracy. Specifically, the MAE metric clearly showed that C7 was the optimal current combination for reproducing DX drifter trajectories, and the NCLS metric also indicated the best performance for C7, except at early times less than 10 days (Table 4).

For PTM-DO, the variation in performance across the different forcing combinations was less pronounced than for PTM-DX. Among the two-component combinations, as with PTM-DX particles, adding windage (C4) resulted in better accuracy than the other two-component combinations. Among the three-component combinations, the inclusion of Ekman current and windage (C6) yielded the highest accuracy, while the combination of Ekman current and Stokes drift (C5) performed the worst. The simulation that included all four current components (C8) consistently demonstrated the best overall performance based on both MAE and NCLS metrics across all evaluated time steps.

4 Discussions

4.1 Optimal forcing combinations and ocean models

From the drifter and particle observations in the EJS, the C7 forcing combination (geostrophic current, Stokes drift, and windage) provided the best performance for PTM-DX particels, while C8 (geostrophic current, Ekman current, Stokes drift, and windage) was most accurate for PTM-DO particles. These performances persisted throughout the simulation, as shown by the temporal evolution of MAE and NCLS metrics in Fig. 9. PTM-DX particles exhibited greater variability in MAE and NCLS across forcing combinations compared to PTM-DO particles, likely due to their stronger sensitivity to wind forcing. The influence of wind enables PTM-DX particles to cross mean current streamlines and transition between eddies, leading to higher uncertainty depending on the applied forcings. For PTM-DX particles, the C1 and C2 cases (solid black and red dash-dot lines in Fig. 9) produced the highest MAE, which appeared to plateau after approximately 50 days, reaching around 600 km. In contrast, cases that included windage (C6, C7, and C8) consistently yielded the lowest MAE, as the accurate estimation of early trajectories near the hyperbolic point possibly contributed to more accurate downstream paths. The abrupt increase in MAE and corresponding drop in NCLS around day 10 corresponds to the period when particles passed near the hyperbolic point (approximately 130°E, 37°N in Fig. 2), a region known for flow divergence and elevated uncertainty in Lagrangian particle fate.

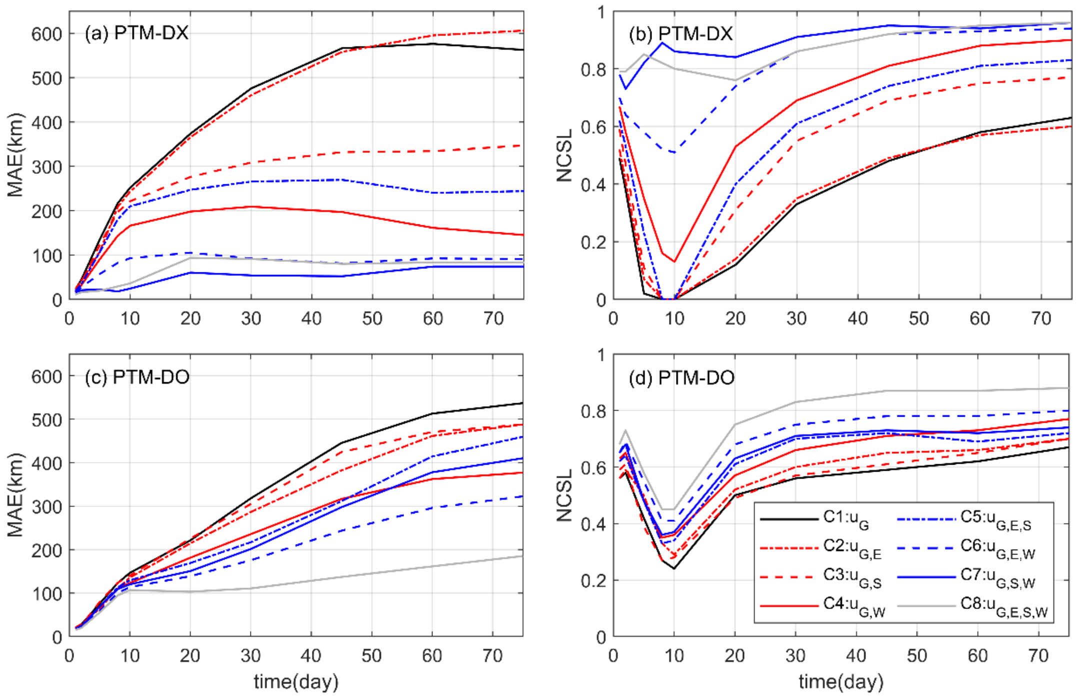

Figure 9. Temporal evolution of MAE for PTM-DX simulations (a) and PTM-DO simulations (c), and temporal evolution of NCLS for PTM-DX simulations (b) and PTM-DO simulations (d) for different forcing combinations (C1-C8, as listed in Table 1).

In addition to evaluating the performance of forcing combinations composed of independent components described in Table 1, we compared particle trajectories driven by the top surface currents of global ocean models (PTM-OM-DX) with those from PTM-DX simulations using the optimal combination (C7). The temporal variations in MAE and NCLS for the ocean model simulations, based on HYCOM and CMEMS (hereafter HYC and CMS), are presented in Table 5. Windage was incorporated at two levels, denoted as W1 (1.5%) and W2 (3%). When driven solely by the surface currents of the ocean models, all particles near the hyperbolic point followed the coastal path along the EKWC. In contrast, the inclusion of windage caused all HYC particles and the majority of CMS particles to shift toward the offshore path. Overall, the addition of windage improved model accuracy, with W1 producing better results than W2. However, all PTM-OM-DX simulations demonstrated lower accuracy than the PTM-DX simulations using the optimal combination (C7). Furthermore, supplementing CMS-W1 and HYC-W1 with Stokes drift did not lead to further improvement. These findings suggest that particle tracking based solely on ocean model surface currents can introduce bias, particularly when simulating the transport of floating debris ranging from micro- to meso-scale. Therefore, validation against observed shallow surface drifter trajectories is essential for improving the reliability of such simulations.

	day	CMS	CMS-W1	CMS-W2	CMS-W1-ST	HYC	HYC -W1	HYC -W2	HYC-W1-ST
MAE	1	22.0 (2.0)	14.6 (1.4)	8.1 (0.8)	5.5 (0.5)	25.2 (2.3)	14.6 (1.4)	13.4 (1.2)	15.5 (1.4)
	5	134.9 (6.1)	43.6 (2.0)	40.1 (1.8)	39.2 (1.8)	76.8 (3.5)	25.8 (1.2)	30.3 (1.4)	21.7 (1.0)
	10	237.0 (9.8)	69.0 (2.9)	64.7 (2.7)	60.0 (2.5)	174.4 (7.2)	32.1 (1.3)	61.0 (2.5)	26.5 (1.1)
	30	415.9 (7.7)	72.0 (1.3)	165.8 (3.1)	150.7 (2.8)	234.7 (4.3)	158.1 (2.9)	201.7 (3.7)	156.1 (2.9)
	75	413.6 (5.6)	126.6 (1.7)	175.7 (2.4)	163.7 (2.2)	182.7 (2.5)	195.4 (2.6)	201.7 (2.7)	163.4 (2.2)
	avg.	244.7 (6.2)	65.2 (1.9)	90.9 (2.2)	83.8 (2.3)	138.8 (4.0)	85.2 (1.9)	101.6 (2.3)	76.64 (2.1)
NCLS	1	0.52 (1.3)	0.70 (1.1)	0.84 (0.9)	0.87 (1.1)	0.52 (1.3)	0.72 (1.1)	0.74 (1.1)	0.71 (0.9)
	5	0.02 (2.0)	0.67 (1.2)	0.70 (1.1)	0.71 (0.9)	0.39 (1.5)	0.80 (1.0)	0.75 (1.1)	0.83 (1.0)
	10	0.00 (2.0)	0.62 (1.3)	0.63 (1.3)	0.64 (0.7)	0.05 (1.9)	0.82 (1.0)	0.64 (1.3)	0.85 (1.0)
	30	0.41 (1.5)	0.89 (1.0)	0.76 (1.2)	0.78 (0.9)	0.65 (1.3)	0.74 (1.2)	0.74 (1.2)	0.74 (0.8)
	75	0.72 (1.3)	0.91 (1.1)	0.94 (1.0)	0.95 (1)	0.87 (1.1)	0.92 (1.0)	0.95 (1.0)	0.95 (1.0)
	avg.	0.33 (1.6)	0.76 (1.1)	0.77 (1.1)	0.79 (0.9)	0.50 (1.4)	0.80 (1.1)	0.76 (1.1)	0.82 (0.9)

Table 5. MAE and NCLS values for the PTM for undrogued particles (PTM-DX) driven by global ocean model outputs (HYCOM and CMEMS) with and without additional Stokes drift and windage effects. HYC and CMS represent HYCOM and CMEMS outputs, respectively. W1 indicates the addition of 1.5% windage effect, and W2 indicates the addition of 3% windage effect, and ST indicates the addition of Stokes drift. Values in parentheses represent the ratio of the MAE and NCLS values to those of C7 (optimal combined forcing for DX) for the corresponding time step. Lower MAE values and higher NCLS values indicate better model accuracy.

https://doi.org/10.5194/egusphere-2026-943
Preprint. Discussion started: 24 February 2026

4.2 Seasonal variation of atmospheric and oceanic forcings

The seasonal variation of waves and winds that potentially influence the transport of floating debris is illustrated in Fig. 10. Both significant wave height (SWH) and wind speed follow a clear seasonal pattern, increasing in the order of summer (June-August), fall (September-November), spring (March-May), and winter (December-February). During fall and winter (Fig. 10g and 10h), the EJS is subject to persistent and strong northwesterly winds, which generate significantly higher wave heights near the Japanese coastline due to fetch-limited wave development from the Korean Peninsula (Chen et al., 2002; Park et al., 2005; Ebuchi, 1999). Monthly averaged satellite-derived SWHs show a pronounced seasonal variability, with high values exceeding 2.5 m in winter and low values below 1 m in summer (Woo and Park, 2017), consistent with the seasonal averages depicted in Fig. 10. This spatial asymmetry in wave height enhances wave-driven surface transport (Stokes drift) toward the Japanese coast during winter. The mean winter SWH reaches 1.68 m, with a maximum of 2.58 m. In contrast, during summer, the mean SWH decreases to 0.55 m, with a peak of 0.82 m, and wave propagation is influenced by prevailing southerly winds, which tend to shift northward.

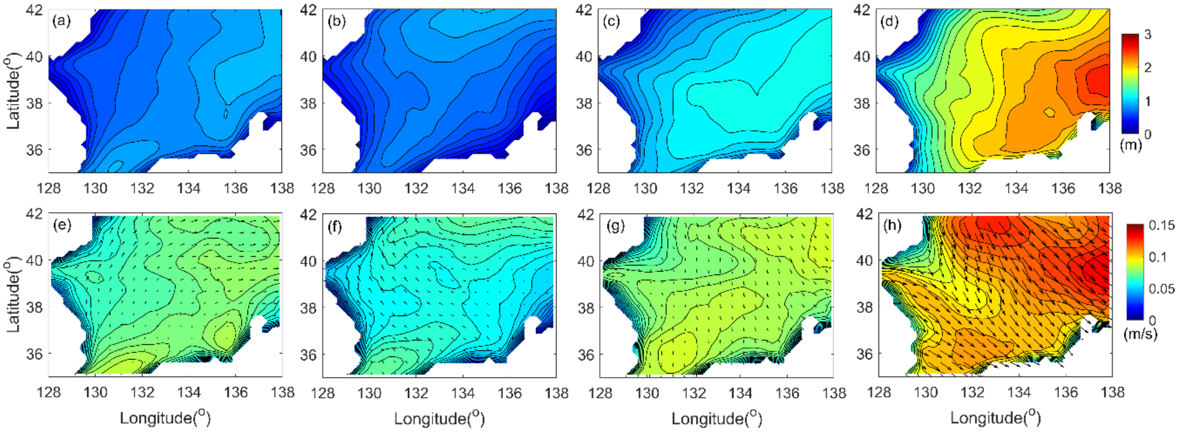

Figure 10. The mean of significant wave height (a-d), wind (e-f) in EJS for each season in 2021: (a,e) spring (March 01-May 30), (b,f) summer (June 01-August 30), (c,g) autumn (Septemper 01-November 30), and (d,h) winter (December 01-Febnuary 28).

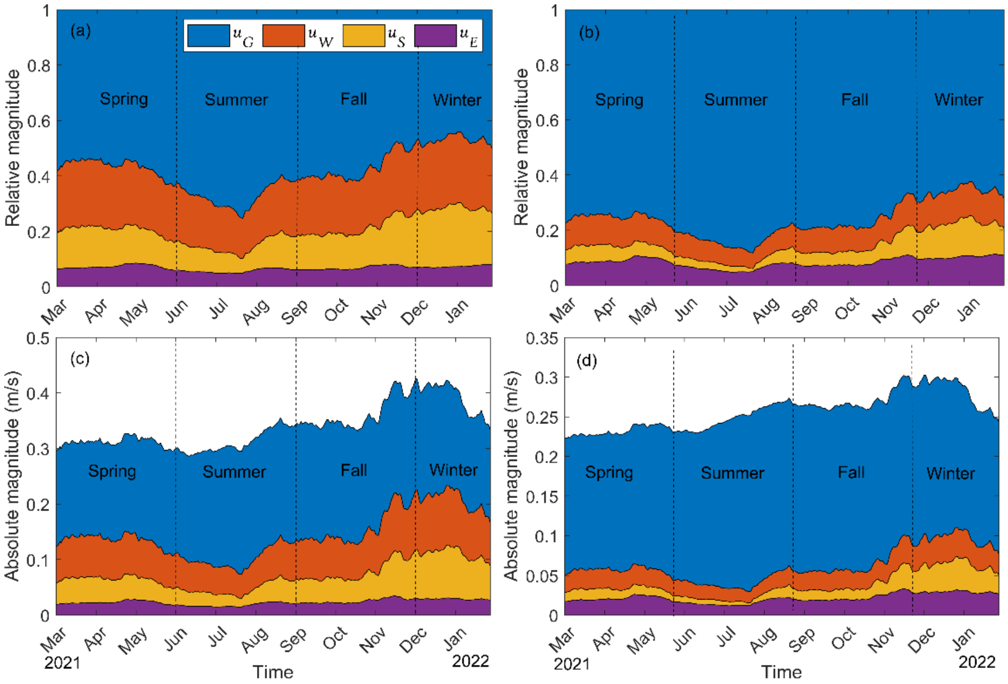

Figure 11. The raletive and absolute value of the current components at the surface (a,c) and 1.5m- depth (b,d) of (u_G-geostrophic current, u_W-wind-driver current, u_S-Stoke current and u_E-Ekman current) from March 2021 to February 2022.

Like the distinct seasonal variations in wave and wind strength and direction, the direct forcings driving surface debris transport also exhibited marked seasonal variability. Figure 11 presents the absolute and relative magnitudes of the forcing components for PTM-DX (Fig. 11a, and c) and PTM-DO (Fig. 11b, and d). For PTM-DX forcings, the geostrophic current was the dominant component year-round, contributing approximately 68% of the total forcing in summer and declining to around 48 % in winter. Among the remaining components, windage and Stokes drift made comparable contributions, both substantially exceeding that of the Ekman current across all seasons. Similarly, for PTM-DO, the geostrophic current remained the primary forcing component, contributing about 83% in summer and decreasing to roughly 65% in winter. The other three components, windage, Stokes drift, and Ekman current, had similar magnitudes, particularly during winter. However, Stokes drift was generally less influential than windage and Ekman current, likely due to its more rapid exponential decay with depth (e^{-2kz}), in contrast to the slower decay of the Ekman current ($e^{-z/d}$). The estimated Ekman depth ranged from approximately 15 m in summer to 30 m in winter, substantially deeper than the depth affected by Stokes drift. Consequently, the absolute magnitude of the Ekman current contribution showed little variation between PTM-DX and PTM-DO.

The PTM results indicate that the optimal current representation for tracking DX drifters is achieved using three components: geostrophic current, Stokes drift, and windage. This combination performed slightly better than the full four-component setup, suggesting potential redundancy or overestimation when the Ekman current is included in modeling surface debris transport. In contrast, the optimal configuration for PTM-DO involved all four components, indicating that at subsurface depths, overlap among wind-driven forcings, such as windage, Stokes drift, and the Ekman current, is reduced, and their combined influence is necessary to achieve the best performance.

4.3 Seasonal variation of paticle transport and dispersion

The seasonal variation of atmospheric and oceanic forcings near the air–sea interface, as described in the previous section, plays a key role in determining the fate of floating debris in the EJS. To investigate the seasonal variability in floating debris dispersion and transport driven by surface forcings, a particle tracking model was run using the optimal forcing combination for DX drifters (C7). A total of 576 particles were released at the ocean surface near the southwestern entrance to the EJS, with releases occurring every five days throughout the year (March 2021 to February 2022), and each particle was tracked for five months. Figure 13 presents streamlines based on seasonally averaged velocity fields (Fig. 13a, c, e, and g), along with the corresponding seasonal particle accumulation maps (Fig. 13b, d, f, and h), showing the relative frequency of particle presence within 5 km grid cells. The three red streamlines highlight trajectories passing through the same points along the eastern side of the subpolar front near 40°N.

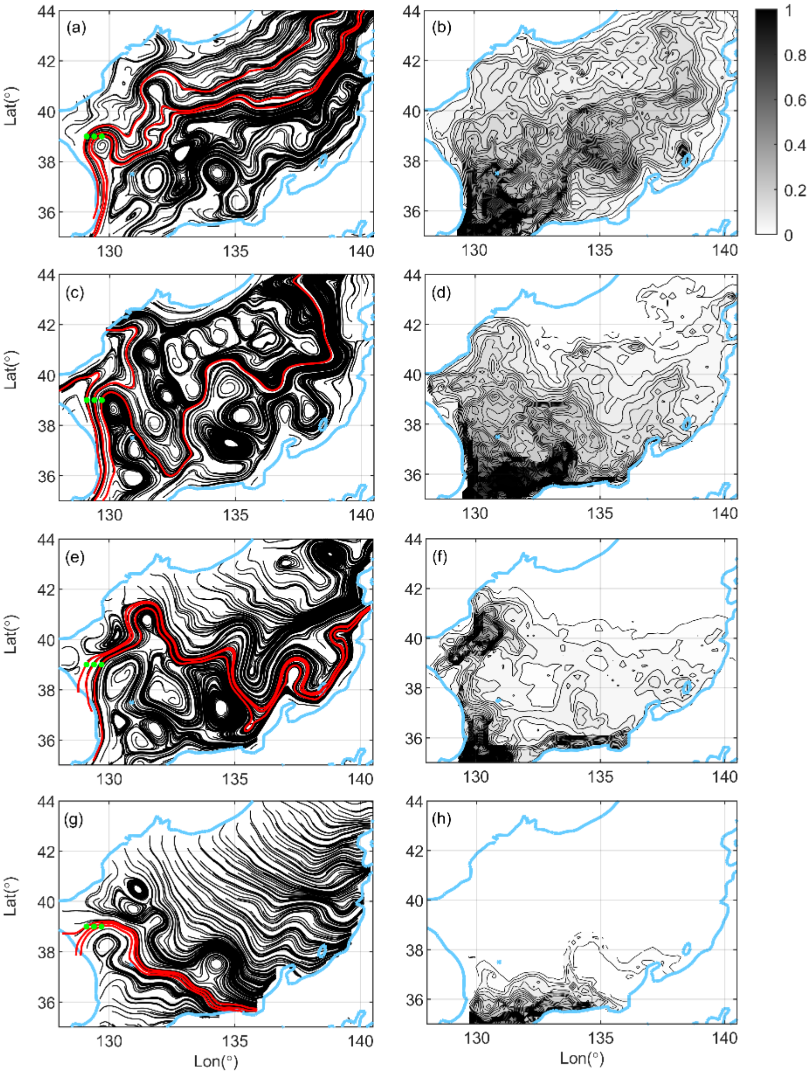

Figure 12. Seasonal streamlines and particle accumulation maps from March 2021 to February 2022, simulated using the optimal forcing combination (C7). Panels (a, c, e, g) show streamlines of the seasonally averaged surface current for spring (March–May), summer (June–August), autumn (September–November), and winter (December–February), respectively. Panels (b, d, f, h) show the corresponding seasonal particle accumulation maps. Red lines represent streamlines that pass through three fixed points marked in green. Particles were released every five days from March 2021 to February 2022 at the southwestern entrance of the EJS and tracked for five months. The accumulation maps display the relative frequency of particle occurrence, calculated as the number of particle passages through each 5 km grid cell normalized by the maximum frequency.

In spring (Fig. 12a, and b), the streamlines reveal that relatively strong winds blow northward near the Korean Peninsula and shift northeastward, especially in the northern EJS, facilitating material transport along and above the subpolar front. This wind-driven configuration results in the broadest dispersion of floating debris among all seasons. In summer (Fig. 12c, and d), the flow is characterized by eddy-like coherent patterns throughout the EJS, driven by persistent mesoscale circulations under the weakest wind conditions. A branch of the EKWC flows northward along the coast and forms a closed streamline loop in the northern coastal region. This circulation pattern suggests that particles entrained on the western side of the EKWC become trapped and accumulate along the Korean coastline. In fall (Fig. 12e, and f), streamlines originating from the northern coastline extend southeastward across the northern EJS. The red streamlines show minimal variation, indicating relatively slow northward particle movement. This is consistent with the broader, lower-concentration particle distributions observed in the accumulation map. Additionally, the streamlines near the Japanese coastline remain open, allowing debris to continue along the coast. In winter (Fig. 12g, and h), most streamlines appear nearly straight, influenced by strong and consistent west-northwesterly winds and wave propagation in the same direction. As a result, particle trajectories are largely confined to the southern EJS. Given that our drifters were released in mid-November and tracked for several months, the fall and winter transport maps (Fig. 12e, f and Fig. 12g, h) effectively represent the observed fate of drifters that eventually beached along the Japanese coastline.

The seasonal beaching locations of particles are illustrated in Fig. 13, where beaching is defined as particle contact with the coastline. In spring (Fig. 13a), the number of beached particles was the lowest among all seasons, with a substantial portion remaining offshore. This pattern corresponds with the springtime streamline plots, which show predominantly northeastward transport across the EJS and limited streamline closure near the coast. In summer (Fig. 13b), when winds were weakest, the widest spatial distribution of beaching was observed, with particles reaching both the Japanese and Korean coastlines surrounding the EJS. Fall (Fig. 13c) was characterized by concentrated beaching along the southern coasts of both Japan and Korea, with particularly pronounced accumulation along the Japanese coastline. In winter (Fig. 13d), strong northwesterly winds likely contributed to increased beaching intensity along the southern Japanese coast. These seasonal mechanisms align with previous numerical studies: Yoon et al. (2010) highlighted the dominant role of monsoonal winds and windage in driving seasonal peaks of floating debris accumulation along the Japanese coast, while Iwasaki et al. (2017) demonstrated that intensified winter wave conditions and associated Stokes drift significantly enhance the onshore transport of buoyant debris toward Japan.

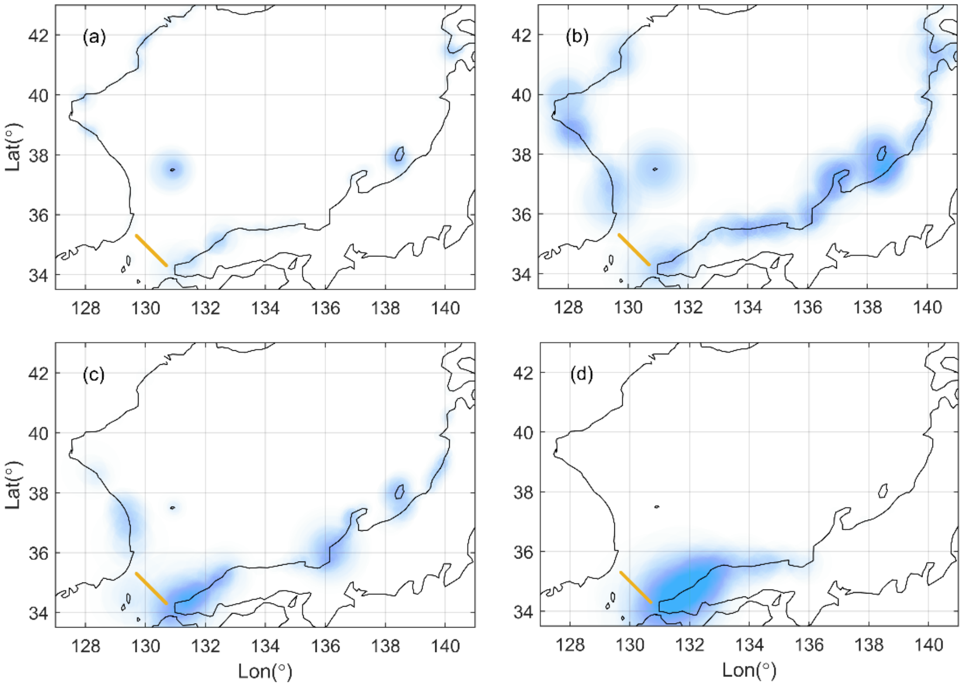

Figure 13. Spatial distribution and relative accumulation intensity of beached particles simulated using the optimal surface forcing (C7) for (a) spring (March–May), (b) summer (June–August), (c) fall (September–November), and (d) winter (December–February). The beached particle locations were determined from the same particle trajectories used in Fig. 12. Beaching is defined as the behavior of particles first contacting the coastline. The particle release location is marked by the yellow line. Color intensity along the coastline indicates the relative density of particle accumulation, with darker shades representing higher accumulation.

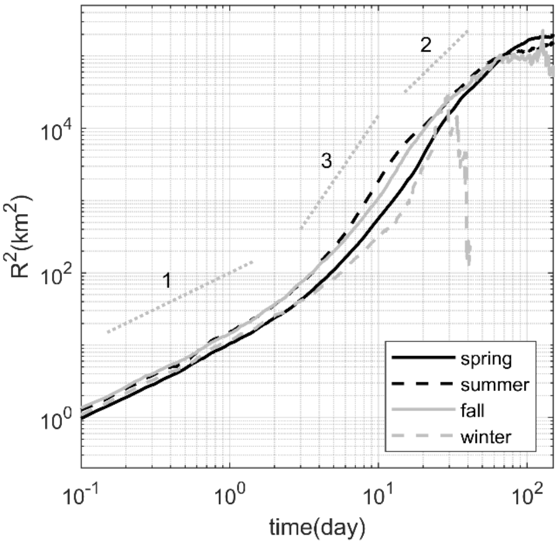

Figure 14. Seasonal variation of relative dispersion, R^2 (t), for particles (same as those used in Fig. 12, and 13) simulated using the optimal forcing combination (C7). Lines indicate relative dispersion for particles released in spring (black solid), summer (black dashed), autumn (gray solid), and winter (gray dashed).

The seasonal variation in relative dispersion can also be interpreted in terms of atmospheric and oceanic forcings (Fig. 14). In all cases, dispersion initially exhibited a brief period of slow growth, attributed to the model's constant diffusivity within grid cells, followed by a more rapid increase consistent with Richardson-like behavior, continuing until approximately 30 days after release. During this phase, particles released in winter showed the lowest relative dispersion, while those released in summer exhibited the highest. The reduced dispersion in winter likely resulted from persistent strong winds and waves that constrained particle motion, leading to concentrated beaching along the southern Japanese coast (Fig. 13d). In contrast, the enhanced dispersion in summer was attributed to weak winds, resulting in reduced wave action, Stokes drift, and Ekman currents, which allow mesoscale eddies to dominate particle transport. This pattern aligns with Fig. 13b, which shows widespread beaching along both the Korean and Japanese coastlines. Over time, relative dispersion in all seasons began to plateau roughly one month after release, as particle pair separations approach the basin scale. These results suggest that strong winds suppress the influence of mesoscale eddies by restructuring the flow into a more uniform, wind-driven (ballistic-like) velocity field, whereas weak winds allow particles to remain entrained within mesoscale eddies, thereby enhancing basin-wide dispersion, especially in marginal seas like the EJS.

5 Conclusions

This study provided a comprehensive assessment of optimal surface forcing configurations for simulating the transport of floating debris in the EJS using a drifter-validated particle tracking model. The largest surface drifter experiment in the EJS was conducted in November 2021, releasing surface drifters near the southwestern entrance of the basin. All surviving drifters eventually beached on the opposite side of the marginal sea, along the southern Japanese coastline. The horizontal diffusivity reaching up to 2,000 m^2/s and saturated at a length scale larger than 200 km, which is 1/10 of the EJS basin scale. These drifter trajectories served as benchmarks to evaluate the performance of various surface forcing combinations, with model accuracy assessed using MAE and NCLS metrics. Among the tested configurations, the forcing combination including geostrophic currents, Stokes drift, and windage (C7) most accurately reproduced the trajectories of undrogued surface drifters (DX). In contrast, the full four-component combination - geostrophic current, Ekman current, Stokes drift, and windage (C8) - achieved the best performance for drogued drifters (DO). The optimized configurations outperformed global ocean circulation models such as HYCOM and CMEMS, which failed to resolve critical bifurcations in early-stage dispersion, particularly near the hyperbolic point. Seasonal simulations using the optimal forcing combinations revealed pronounced variability in the fate of floating debris. In winter, strong northwesterly winds and wave-induced processes drove particles to accumulate along the southern Japanese coastline. In contrast, weaker summer winds allowed mesoscale eddies to dominate, resulting in broader dispersal and more balanced beaching along both the Korean and Japanese coasts. Although a limited number of drifters were used, this experiment provides a unique dataset demonstrating potential transport scenarios for floating debris across a marginal sea, aiding in the understanding of debris accumulation along the coastline, and identifying the optimal current combinations for tracking debris submerged near the surface.

Data availability

All datasets and models used in this study are publicly available to support transparency and reproducibility. Geostrophic currents were obtained from the Copernicus Marine Service product SEALEVEL_GLO_PHY_L4_MY_008_047 (https://data.marine.copernicus.eu/product/SEALEVEL_GLO_PHY_L4_MY_008_047/description). Wind velocity at 10 m height was sourced from the ECMWF ERA5 reanalysis provided by ECMWF (https://cds.climate.copernicus.eu/datasets/reanalysis-era5-single-levels?tab=overview). Stokes drift fields were computed using the University of Miami Wave Model (https://github.com/umwm/umwm). HYCOM data were obtained from https://www.hycom.org/data/glby0pt08/expt-93pt0, and CMEMS data were downloaded from the Copernicus Marine Service product GLOBAL_MULTIYEAR_PHY_001_030 (https://data.marine.copernicus.eu/product/GLOBAL_MULTIYEAR_PHY_001_030/description). Drifter data in the East/Japan Sea is available at https://drive.google.com/file/d/15IpunKfFTN9H7z2Ww6l_ihqniNy8Rr2M/view?usp=drive_link. All trajectory analyses, and visualizations were conducted using MATLAB R2022a.

Author contributions

JMC initiated the research idea, while HTMT developed the study design and carried out the research under the guidance and scholarly discussions with JMC and YGP. The formal analysis was performed by HTMT in collaboration with JMC. The manuscript was drafted by HTMT and subsequently reviewed and revised by JMC. All authors contributed to the conceptual development and refinement of the study.

Competing interests

The authors declare there are no conflicts of interest for this manuscript

Financial support

This research was supported by the Korea Institute of Marine Science & Technology Promotion (KIMST) funded by the Ministry of Oceans and Fisheries (20220546).

References

Amante, C., & Eakins, B. W. (2009). ETOPO1 Global Relief Model converted to PanMap layer format. *ETOPO1 Global Relief Model converted to PanMap layer format.*, *24*, 19.

Aurell, E., Boffetta, G., Crisanti, A., Paladin, G., & Vulpiani, A. (1996). Predictability in systems with many characteristic times: The case of turbulence. *Physical Review E*, *53*(3), 2337.

Bressan, A. C. (2019). The Deflection Angle of Surface Ocean Currents From the Wind Direction. *Journal of Geophysical Research: Oceans*, *124*(11), 7412–7420. doi: https://doi.org/10.1029/2019JC015454.

Callies, U., Groll, N., Horstmann, J., Kapitza, H., Klein, H., Maßmann, S., & Schwichtenberg, F. (2017). Surface drifters in the German Bight: model validation considering windage and Stokes drift. Ocean Science, 13(5), 799-827.

Castellari, S., Griffa, A., Özgökmen, T. M., & Poulain, P. M. (2001). Prediction of particle trajectories in the adriatic sea using Lagrangian data assimilation. *Journal of Marine Systems*, *29*(1–4), 33–50. doi: 10.1016/S0924-7963(01)00008-2.

Chen, F., Zhang, C., Brett, M. T., & Nielsen, J. M. (2020). The importance of the wind-drag coefficient parameterization for hydrodynamic modeling of a large shallow lake. *Ecological Informatics*, *59*, 101106. doi: 10.1016/j.ecoinf.2020.101106.

Chen, G., Chapron, B., Ezraty, R., Vandemark, D., 2002. A global view of swell and wind sea climate in the ocean by satellite altimeter and scatterometer. J. Atmos. Ocean. Technol. 19 (11), 1849–1859.

Chenillat, F., Huck, T., Maes, C., Grima, N., & Blanke, B. (2021). Fate of floating plastic debris released along the coasts in a global ocean model. *Marine Pollution Bulletin*, *165*, 112116. doi: 10.1016/j.marpolbul.2021.112116.

Choi, J., Troy, C., Hawley, N., McCormick, M., & Wells, M. (2020). Lateral dispersion of dye and drifters in the center of a very large lake. Limnology and Oceanography, 65(2), 336-348.

https://doi.org/10.5194/egusphere-2026-943
Preprint. Discussion started: 24 February 2026

Clark, B. L., Carneiro, A. P. B., Pearmain, E. J., Rouyer, M. M., Clay, T. A., Cowger, W., Phillips, R. A., Manica, A., Hazin, C., Eriksen, M., González-Solís, J., Adams, J., Albores-Barajas, Y. V., Alfaro-Shigueto, J., Alho, M. S., Araujo, D. T., Arcos, J. M., Arnould, J. P. Y., Barbosa, N. J. P., … Dias, M. P. (2023). Global assessment of marine plastic exposure risk for oceanic birds. *Nature Communications*, *14*(1), 3665. doi: 10.1038/s41467-023-38900-z.

Cole, M., Lindeque, P., Halsband, C., & Galloway, T. S. (2011). Microplastics as contaminants in the marine environment: A review. *Marine Pollution Bulletin*, *62*(12), 2588–2597. doi: 10.1016/j.marpolbul.2011.09.025.

Cózar, A., Echevarría, F., González-Gordillo, J. I., Irigoien, X., Úbeda, B., Hernández-León, S., Palma, Á. T., Navarro, S., García-de-Lomas, J., Ruiz, A., Fernández-de-Puelles, M. L., & Duarte, C. M. (2014). Plastic debris in the open ocean. *Proceedings of the National Academy of Sciences of the United States of America*, *111*(28), 10239–10244. doi: 10.1073/pnas.1314705111.

Curcic, M., Chen, S. S., & Özgökmen, T. M. (2016). Hurricane-induced ocean waves and stokes drift and their impacts on surface transport and dispersion in the Gulf of Mexico. *Geophysical Research Letters*, *43*(6), 2773-2781.

Cushman-Roisin, B., & Beckers, J. M. (2011). *Introduction to geophysical fluid dynamics: physical and numerical aspects* (Vol. 101). Academic press.

D'Asaro, E. A., Shcherbina, A. Y., Klymak, J. M., Molemaker, J., Novelli, G., Guigand, C. M., ... & Özgökmen, T. M. (2018). Ocean convergence and the dispersion of flotsam. Proceedings of the National Academy of Sciences, 115(6), 1162-1167.

Dobler, D., Maes, C., Martinez, E., Rahmania, R., Gautama, B. G., Farhan, A. R., & Dounias, E. (2022). On the Fate of Floating Marine Debris Carried to the Sea through the Main Rivers of Indonesia. *Journal of Marine Science and Engineering*, *10*(8), 1009. doi: 10.3390/jmse10081009.

Ebuchi, N. (1999). Growth of wind waves with fetch in the Sea of Japan under winter monsoon investigated using data from satellite altimeters and scatterometer. *Journal of Oceanography*, *55*(5), 575-584.

Gu, J., Zhang, Y., Tuo, P., Hu, Z., Chen, S., & Hu, J. (2024). Surface floating objects moving from the Pearl River Estuary to Hainan Island: An observational and model study. *Journal of Marine Systems*, *241*. doi: 10.1016/j.jmarsys.2023.103917.

Haza, A. C., Paldor, N., Özgökmen, T. M., Curcic, M., Chen, S. S., & Jacobs, G. (2019). Wind-Based Estimations of Ocean Surface Currents From Massive Clusters of Drifters in the Gulf of Mexico. *Journal of Geophysical Research: Oceans*, *124*(8), 5844–5869. doi: 10.1029/2018JC014813.

Hersbach, H., Bell, B., Berrisford, P., Hirahara, S., Horányi, A., Muñoz-Sabater, J., ... & Thépaut, J. N. (2020). The ERA5 global reanalysis. *Quarterly journal of the royal meteorological society*, *146*(730), 1999-2049.

Hsu, P. C., Centurioni, L., Shao, H. J., Zheng, Q., Lu, C. Y., Hsu, T. W., & Tseng, R. S. (2021). Surface current variations and oceanic fronts in the southern East China Sea: Drifter experiments, coastal radar applications, and satellite observations. Journal of Geophysical Research: Oceans, 126(10), e2021JC017373.

Huang, G., Zhan, H., He, Q., Wei, X., & Li, B. (2021). A Lagrangian study of the near-surface intrusion of Pacific water into the South China Sea. *Acta Oceanologica Sinica*, *40*(7), 15–30. doi: 10.1007/s13131-021-1766-6.

Hui, J., Sato, T., & Kanao, S. (2023). Numerical estimation of the hotspot positions of floating plastic debris in the Tsushima Strait using the adjoint marginal sensitivity method. *Ocean Engineering*, *270*(December 2022), 113606. doi: 10.1016/j.oceaneng.2022.113606.

Ichiye, T. (1984). Some problems of circulation and hydrography of the Japan Sea and the Tsushima Current. In *Elsevier oceanography series* (Vol. 39, pp. 15-54). Elsevier.

Irfan, T., Isobe, A., & Matsuura, H. (2024). A particle tracking model approach to determine the dispersal of riverine plastic debris released into the Indian Ocean. *Marine Pollution Bulletin*, *199*, 115985. doi: 10.1016/j.marpolbul.2023.115985.

Isobe, A., Uchida, K., Tokai, T., & Iwasaki, S. (2015). East Asian seas: A hot spot of pelagic microplastics. *Marine Pollution Bulletin*, *101*(2), 618–623. doi: 10.1016/j.marpolbul.2015.10.042.

Iwasaki, S., Isobe, A., Kako, S., Uchida, K., & Tokai, T. (2017). Fate of microplastics and mesoplastics carried by surface currents and wind waves: A numerical model approach in the Sea of Japan. *Marine Pollution Bulletin*, *121*(1–2), 85–96. doi: 10.1016/j.marpolbul.2017.05.057.

Jalón-Rojas, I., Wang, X. H., & Fredj, E. (2019). A 3D numerical model to Track Marine Plastic Debris (TrackMPD): Sensitivity of microplastic trajectories and fates to particle dynamical properties and physical processes. *Marine Pollution Bulletin*, *141*, 256–272. doi: 10.1016/j.marpolbul.2019.02.052.

Jeon, C., Park, J.-H., Varlamov, S. M., Yoon, J.-H., Kim, Y. H., Seo, S., Park, Y.-G., Min, H. S., Lee, J. H., & Kim, C.-H. (2014). Seasonal variation of semidiurnal internal tides in the East/Japan Sea. *Journal of Geophysical Research: Oceans*, *119*(5), 2843– 2859. doi: doi:10.1002/2014JC009864.

Kako, S., Isobe, A., Yoshioka, S., Chang, P. H., Matsuno, T., Kim, S. H., & Lee, J. S. (2010). Technical issues in modeling surface-drifter behavior on the East China Sea shelf. *Journal of Oceanography*, *66*(2), 161–174. doi: 10.1007/s10872-010-0014-z.

Kim, J. C., Yu, D. H., Sim, J. E., Son, Y. T., Bang, K. Y., & Shin, S. (2023). Validation of OpenDrift-Based Drifter Trajectory Prediction Technique for Maritime Search and Rescue. *Journal of Ocean Engineering and Technology*, *37*(4), 145–157. doi: 10.26748/KSOE.2023.018.

Kim, K., Kim, K. R., Min, D. H., Volkov, Y., Yoon, J. H., & Takematsu, M. (2001). Warming and structural changes in the East (Japan) Sea: a clue to future changes in global oceans?. *Geophysical Research Letters*, *28*(17), 3293-3296.

Kim, K., Tran, H. T. M., Song, K. M., Son, Y. B., Park, Y. G., Ryu, J. H., ... & Choi, J. M. (2024). Near-Surface Dispersion and Current Observations Using Dye, Drifters, and HF Radar in Coastal Waters. Remote Sensing, 16(11), 1985.

Kim, Y. R., Kang, D. W., Lee, S., Choi, K. Y., Kim, H. E., Jung, J. M., ... & Kim, C. J. (2021). Distribution and assessment of heavy metal concentrations in the East Sea-Byeong ocean dumping site, Korea. *Marine Pollution Bulletin*, *172*, 112815.

Kuroda, M., Isobe, A., Uchida, K., Tokai, T., Kitakado, T., Yoshitake, M., Miyamoto, Y., Mukai, T., Imai, K., Shimizu, K., Yagi, M., Mituhasi, T., & Habano, A. (2024). Abundance and potential sources of floating polystyrene foam macro- and microplastics around Japan. *Science of the Total Environment*, *925*(November 2023), 171421. doi: 10.1016/j.scitotenv.2024.171421.

LaCasce, J. H. (2008), Statistics from Lagrangian observations, Prog. Oceanogr., 77,1–29, doi:10.1016/j.pocean.2008.02.002.

Lebreton, L. (2022). The status and fate of oceanic garbage patches. *Nature Reviews Earth & Environment*, *3*(11), 730–732. doi: https://doi.org/10.1038/s43017-022-00363-z.

Lebreton, L. C. M., Greer, S. D., & Borrero, J. C. (2012). Numerical modelling of floating debris in the world's oceans. *Marine Pollution Bulletin*, *64*(3), 653–661. doi: 10.1016/j.marpolbul.2011.10.027.

Lee, Dong Kyu, & Niiler, P. (2010). Eddies in the southwestern East/Japan Sea. *Deep-Sea Research Part I: Oceanographic Research Papers*, *57*(10), 1233–1242. doi: 10.1016/j.dsr.2010.06.002.

Liang, J. H., Liu, J., Benfield, M., Justic, D., Holstein, D., Liu, B., Hetland, R., Kobashi, D., Dong, C., & Dong, W. (2021). Including the effects of subsurface currents on buoyant particles in Lagrangian particle tracking models: Model development and its application to the study of riverborne plastics over the Louisiana/Texas shelf. *Ocean Modelling*, *167*(August), 101879. doi: 10.1016/j.ocemod.2021.101879.

Liu, Y., Weisberg, R. H., Vignudelli, S., & Mitchum, G. T. (2014). Evaluation of altimetry-derived surface current products using Lagrangian drifter trajectories in the eastern Gulf of Mexico. *Journal of Geophysical Research: Oceans*, *119*(5), 2827–2842. doi: 10.1002/2013JC009710.

Liu, Yonggang, & Weisberg, R. H. (2011). Evaluation of trajectory modeling in different dynamic regions using normalized cumulative Lagrangian separation. *Journal of Geophysical Research: Oceans*, *116*(C9). doi: 10.1029/2010JC006837.

Liubartseva, S., Coppini, G., Lecci, R., & Clementi, E. (2018). Tracking plastics in the Mediterranean: 2D Lagrangian model. *Marine Pollution Bulletin*, *129*(1), 151–162. doi: 10.1016/j.marpolbul.2018.02.019.

Mao, Y., & Heron, M. L. (2008). The influence of fetch on the response of surface currents to wind studies by HF ocean surface radar. *Journal of Physical Oceanography*, *38*(5), 1107–1121. doi: 10.1175/2007JPO3709.1.

Mariano, A. J., Kourafalou, V. H., Srinivasan, A., Kang, H., Halliwell, G. R., Ryan, E. H., & Roffer, M. (2011). On the modeling of the 2010 Gulf of Mexico Oil Spill. *Dynamics of Atmospheres and Oceans*, *52*(1–2), 322–340. doi: 10.1016/j.dynatmoce.2011.06.001.

Maximenko, N., Hafner, J., & Niiler, P. (2012). Pathways of marine debris derived from trajectories of Lagrangian drifters. *Marine Pollution Bulletin*, *65*(1–3), 51–62. doi: 10.1016/j.marpolbul.2011.04.016.

McWilliams, J. C. (2016). Submesoscale currents in the ocean. *Proceedings of the Royal Society A: Mathematical, Physical and Engineering Sciences*, *472*(2189), 20160117. doi: 10.1098/rspa.2016.0117.

Medina-Rubio, J., Nussbaum, M., van den Bremer, T. S., & van Sebille, E. (2026). Using surface drifters to characterise near-surface ocean dynamics in the southern North Sea: a data-driven approach. Ocean Science, 22(1), 49-74.

Nakakuni, M., Nishida, M., Nishibata, R., Kishimoto, K., Yamaguchi, H., Ichimi, K., Ishizuka, M., Suenaga, Y., & Tada, K. (2024). Convergence zones of coastal waters as hotspots for floating microplastic accumulation. *Marine Pollution Bulletin*, *206*(June), 116691. doi: 10.1016/j.marpolbul.2024.116691.

Okubo, A., 1971. Oceanic diffusion diagrams. In: Deep Sea Research and Oceanographic Abstracts, 18, pp. 789–802. https://doi.org/10.1016/0011-7471(71)90046-5.

Onink, V., Wichmann, D., Delandmeter, P., & van Sebille, E. (2019). The Role of Ekman Currents, Geostrophy, and Stokes Drift in the Accumulation of Floating Microplastic. *Journal of Geophysical Research: Oceans*, *124*(3), 1474–1490. doi: 10.1029/2018JC014547.

Ono, J., Ohshima, K. I., Uchimoto, K., Ebuchi, N., Mitsudera, H., & Yamaguchi, H. (2013). Particle-tracking simulation for the drift/diffusion of spilled oils in the Sea of Okhotsk with a three-dimensional, high-resolution model. *Journal of Oceanography*, *69*(4), 413–428. doi: 10.1007/s10872-013-0182-8.

Park, K. A., Chung, J. Y., Kim, K., & Cornillon, P. C. (2005). Wind and bathymetric forcing of the annual sea surface temperature signal in the East (Japan) Sea. *Geophysical Research Letters*, *32*(5).

Park, Y.-G., & Seo, S. (2021). Review on Lagrangian Particle Tracking Modeling for Floating Objects around the Korean Peninsula. *KMI International Journal of Maritime Affairs and Fisheries*, *13*(2), 67–83. doi: 10.54007/ijmaf.2021.13.2.67.

Pärn, O., Davulienė, L., Moy, D. M., Vahter, K., Stips, A., & Torsvik, T. (2023). Effects of Eulerian current, Stokes drift and wind while simulating surface drifter trajectories in the Baltic Sea. *Oceanologia*, *65*(3), 453-465.

Paul, S., Nath, S., Bhattacharjee, S., & Mukherjee, S. (2024). Unveiling the effects of microplastics pollution on marine fauna. *Blue Biotechnology 2024 1:1*, *1*(1), 6. doi: 10.1186/s44315-024-00006-6.

Pinheiro, H. T., MacDonald, C., Santos, R. G., Ali, R., Bobat, A., Cresswell, B. J., Francini-Filho, R., Freitas, R., Galbraith, G. F., Musembi, P., Phelps, T. A., Quimbayo, J. P., Quiros, T. E. A. L., Shepherd, B., Stefanoudis, P. V., Talma, S., Teixeira, J. B., Woodall, L. C., & Rocha, L. A. (2023). Plastic pollution on the world's coral reefs. *Nature*, *619*(7969), 311–316. doi: 10.1038/s41586-023-06113-5.

Poje, A. C., Özgökmen, T. M., Lipphardt Jr, B. L., Haus, B. K., Ryan, E. H., Haza, A. C., ... & Mariano, A. J. (2014). Submesoscale dispersion in the vicinity of the Deepwater Horizon spill. Proceedings of the National Academy of Sciences, 111(35), 12693-12698.

Prants, S. V., Budyansky, M. V., Ponomarev, V. I., & Uleysky, M. Y. (2011). Lagrangian study of transport and mixing in a mesoscale eddy street. *Ocean Modelling*, *38*(1–2), 114–125. doi: 10.1016/j.ocemod.2011.02.008.

Prants, S. V., Ponomarev, V. I., Budyansky, M. V., Uleysky, M. Y., & Fayman, P. A. (2015). Lagrangian analysis of the vertical structure of eddies simulated in the Japan Basin of the Japan/East Sea. *Ocean Modelling*, *86*, 128-140.

Röhrs, J., Sutherland, G., Jeans, G., Bedington, M., Sperrevik, A. K., Dagestad, K. F., Gusdal, Y., Mauritzen, C., Dale, A., & LaCasce, J. H. (2023).

Rypina, Irina I., Getscher, T. R., Pratt, L. J., & Mourre, B. (2021). Observing and Quantifying Ocean Flow Properties Using Drifters with Drogues at Different Depths. *Journal of Physical Oceanography*, *51*(8), 2463–2482. doi: 10.1175/JPO-D-20-0291.1.

Saeedi, M. (2024). How microplastics interact with food chain: a short overview of fate and impacts. *Journal of Food Science and Technology*, *61*(3), 403–413. doi: 10.1007/s13197-023-05720-4.

Santos de Moura, M. & Vianna, M. (2020). A new threat: assessing the main interactions between marine fish and plastic debris from a scientometric perspective. *Reviews in Fish Biology and Fisheries*, *30*(4), 623–636.

Sebille, E. van, Aliani, S., Law, K. L., Maximenko, N., Alsina, J. M., Bagaev, A., Bergmann, M., Chapron, B., Chubarenko, Cózar, I., Andrés, Delandmeter, P., Egger, M., Fox-Kemper, B., Garaba, S. P., Oddijn-Murphy, L., Hardesty, B. D., Matthew J Hoffman17, A. I., Cleo E Jongedijk19, Mikael L A Kaandorp1 , Liliya Khatmullina6, A. A. K., … Giuseppe Suaria2 , Martin Thiel34, 35, 36, T. S. van den B. and D. W. (2020). The physical oceanography of the transport of floating marine debris. *Environmental Research Letters*, *15*(2), 023003. Retrieved from http://dx.doi.org/10.1088/1748-9326/ab6d7d.

Seo, S., Park, Y. G., & Kim, K. (2020). Tracking flood debris using satellite-derived ocean color and particle-tracking modeling. *Marine Pollution Bulletin*, *161*(PA), 111828. doi: 10.1016/j.marpolbul.2020.111828.

Sotillo, M. G., Garcia-Ladona, E., Orfila, A., Rodríguez-Rubio, P., Maraver, J. C., Conti, D., ... & Álvarez-Fanjul, E. (2016). The MEDESS-GIB database: tracking the Atlantic water inflow. Earth System Science Data, 8(1), 141-149.

Sudre, J., Maes, C., & Garçon, V. (2013). On the global estimates of geostrophic and Ekman surface currents. *Limnology and Oceanography: Fluids and Environments*, *3*(1), 1–20. doi: 10.1215/21573689-2071927.

Sun, Z., Hu, J., Lin, H., Chen, Z., Zhu, J., Yang, L., ... & Wu, X. (2022). Lagrangian observation of the Kuroshio current by surface drifters in 2019. Journal of Marine Science and Engineering, 10(8), 1027.

Takeda, H., & Isobe, A. (2024). Quantification of ocean microplastic fragmentation processes in the Sea of Japan using a combination of field observations and numerical particle tracking model experiments. *Marine Pollution Bulletin*, *208*, 117032.

Talley, L.D., D.-H. Min, V.B. Lobanov, V.A. Luchin, V.I. Ponomarev, A.N. Salyuk, A.Y Shcherbina, P.Y. Tishchenko, and I. Zhabin. 2006. Japan/East Sea water masses and their relation to the sea's circulation. *Oceanography* 19(3):32–49, https://doi.org/10.5670/oceanog.2006.42.

Tamtare, T., Dumont, D., & Chavanne, C. (2022). The Stokes drift in ocean surface drift prediction. *Journal of Operational Oceanography*, *15*(3), 156–168. doi: 10.1080/1755876X.2021.1872229.

Tekman, M. B., Walther, B. A., Peter, C., Gutow, L., & Bergmann, M. (2022). Impacts of Plastic Pollution in the Oceans on Marine Species, Biodiversity and Ecosystems Summary of a Study for Wwf By Summary of a Study for Wwf By Wwf International 2022 3 Summary. *Alfred-Wegener-Institut*. doi: 10.5281/zenodo.5898684.

Thiel, M., Luna-Jorquera, G., Álvarez-Varas, R., Gallardo, C., Hinojosa, I. A., Luna, N., Miranda-Urbina, D., Morales, N., Ory, N., Pacheco, A. S., Portflitt-Toro, M., & Zavalaga, C. (2018). Impacts of marine plastic pollution from continental coasts to subtropical gyres-fish, seabirds, and other vertebrates in the SE Pacific. *Frontiers in Marine Science*, *5*(July), 238. doi: 10.3389/fmars.2018.00238.

Yoon, J. H., Kawano, S., & Igawa, S. (2010). Modeling of marine litter drift and beaching in the Japan Sea. *Marine pollution bulletin*, 60(3), 448-463.

Woo, H. J., & Park, K. A. (2017). Long-term trend of satellite-observed significant wave height and impact on ecosystem in the East/Japan Sea. *Deep Sea Research Part II: Topical Studies in Oceanography*, 143, 1-14.

Wu, J. (1982). Wind-stress coefficients over sea surface from breeze to hurricane. *Journal of Geophysical Research: Oceans*, *87*(C12), 9704–9706. doi: 10.1029/jc087ic12p09704.